

Forcing Mechanisms for an Internal Rear-Flank Downdraft Momentum Surge in the 18 May 2010 Dumas, Texas, Supercell

PATRICK S. SKINNER

NOAA/National Severe Storms Laboratory, Norman, Oklahoma

CHRISTOPHER C. WEISS

Texas Tech University, Lubbock, Texas

LOUIS J. WICKER

NOAA/National Severe Storms Laboratory, Norman, Oklahoma

COREY K. POTVIN

Cooperative Institute for Mesoscale Meteorological Studies, University of Oklahoma, and NOAA/National Severe Storms Laboratory, Norman, Oklahoma

DAVID C. DOWELL

NOAA/Earth System Research Laboratory, Boulder, Colorado

(Manuscript received 23 April 2015, in final form 27 July 2015)

ABSTRACT

The forcing and origins of an internal rear-flank downdraft (RFD) momentum surge observed by the second Verification of the Origin of Rotation in Tornadoes Experiment (VORTEX2) within a supercell occurring near Dumas, Texas, on 18 May 2010 is assessed through ensemble Kalman filter (EnKF) storm-scale analyses. EnKF analyses are produced every 2 min from mobile Doppler velocity data collected by the Doppler on Wheels and Shared Mobile Atmospheric Research and Teaching radars, as well as radial velocity and reflectivity data from the KAMA (Amarillo, Texas) WSR-88D. EnKF analyses are found to reproduce the structure and evolution of an internal RFD momentum surge observed in independent mobile Doppler radar observations.

Pressure retrievals of EnKF analyses reveal that the low-level RFD outflow structure is primarily determined through nonlinear dynamic perturbation pressure gradient forcing. Horizontal acceleration into a trough of low perturbation pressure between the low-level mesocyclone and mesoanticyclone and trailing the primary RFD gust front is followed by an abrupt deceleration of air parcels crossing the trough axis. This deceleration and associated strong convergence downstream of the pressure trough and horizontal velocity maximum are indicative of an internal RFD momentum surge. Backward trajectory analyses reveal that air parcels within the RFD surge originate from two source regions: near the surface to the north of the low-level mesocyclone, and in the ambient flow outside of the storm environment at a height of approximately 2 km.

1. Introduction

Considerable recent research has focused on small-scale regions of enhanced horizontal momentum within the rear-flank downdraft (RFD) of supercell thunderstorms,

known as internal RFD momentum surges (or simply RFD surges). RFD surges have been regularly identified in data collected by portable in situ networks (Finley and Lee 2004; Lee et al. 2004; Hirth et al. 2008; Karstens et al. 2010; Lee et al. 2011; Skinner et al. 2011; Lee et al. 2012), remote sensing platforms with high spatial resolution (Wurman et al. 2007; Marquis et al. 2008; Wurman et al. 2010; Marquis et al. 2012; Kosiba et al. 2013; Bluestein et al. 2014; Mahale et al. 2014; Skinner et al. 2014, hereafter S14; Weiss et al. 2014; Houser et al.

Corresponding author address: Patrick Skinner, NOAA/National Severe Storms Laboratory, 120 David L. Boren Blvd., Norman, OK 73072.
E-mail: patrick.skinner@noaa.gov

2015; Kurdzo et al. 2015), and recent numerical simulations (Adlerman 2003; Mashiko et al. 2009; Schenkman et al. 2014a,b; Dahl et al. 2014). These studies have revealed RFD surges behave similarly to an “RFD within an RFD,” with enhanced convergence along the leading edge of the momentum surge (Wurman et al. 2007; Marquis et al. 2008; Wurman et al. 2010; Lee et al. 2012; Marquis et al. 2012; Kosiba et al. 2013), the low-level mesocyclone trailing and to the left of the surge apex (Marquis et al. 2008; Mashiko et al. 2009; Karstens et al. 2010; Wurman et al. 2010; Lee et al. 2011, 2012; Marquis et al. 2012; Kosiba et al. 2013; Schenkman et al. 2014b; Mahale et al. 2014; S14; Weiss et al. 2014), and thermodynamic characteristics within the surge differing from those in the broadscale RFD (Finley and Lee 2004; Lee et al. 2004; Hirth et al. 2008; Lee et al. 2011; Skinner et al. 2011; Lee et al. 2012; S14). Observations of arching vortex lines connecting counter-rotating vortices meridionally straddling the leading edge of an internal RFD momentum surge (Marquis et al. 2012; Kosiba et al. 2013) imply that tilting of baroclinically generated vorticity within the surge may be an important source of near-surface vertical vorticity (Straka et al. 2007; Markowski et al. 2008; Markowski and Richardson 2014). Additionally, convergence along the internal RFD momentum surge gust front has been found to promote the radially inward transport of angular momentum surrounding the low-level mesocyclone and assist in tornado genesis and maintenance (Marquis et al. 2012; Kosiba et al. 2013). Finally, RFD surges possessing different kinematic (Marquis et al. 2012) or thermodynamic (Lee et al. 2012) characteristics than either prior surges or the broadscale RFD have been found to precede tornado dissipation.

Despite the importance of internal RFD momentum surges to tornado genesis, maintenance, and decay, comparatively little is known about their origins and physical processes responsible for their development. Efforts to diagnose air parcel source regions and four-dimensional forcing of RFD surges are complicated by limited temporal and spatial coverage of mobile in situ and Doppler radar networks typically used in supercell research, in particular the lack of both kinematic observations away from areas of precipitation and thermodynamic observations above the surface (Marquis et al. 2012, 2014). An attractive method for overcoming these observational limitations and retrieving the atmospheric state of supercells is assimilation of Doppler radar data into a numerical cloud model using ensemble Kalman filter (EnKF) techniques (Evensen 1994; Houtekamer and Mitchell 1998). Ensemble Kalman filters use an ensemble of numerical simulations to estimate the background-error covariances needed to combine observations with a model state estimate

in situations where these covariances are expected to vary in time and space and have been shown to produce accurate analyses of supercells in both observing system simulation experiments (OSSEs; Snyder and Zhang 2003; Caya et al. 2005; Tong and Xue 2005; Xue et al. 2006; Yussouf and Stensrud 2010; Potvin and Wicker 2012, 2013a) and real-data case studies (Dowell et al. 2004; Aksoy et al. 2009; Dowell and Wicker 2009; Dowell et al. 2011; Dawson et al. 2012; Marquis et al. 2012; Potvin et al. 2013; Tanamachi et al. 2013; Marquis et al. 2014; Tanamachi et al. 2015). The success of EnKF techniques in retrieving the state of the atmosphere in and surrounding supercells makes them a valuable tool for both probabilistic convective-scale numerical weather prediction (e.g., Stensrud et al. 2013) and analysis of storm-scale processes (Marquis et al. 2012; Potvin et al. 2013; Tanamachi et al. 2013; Marquis et al. 2014; Tanamachi et al. 2015).

This study employs EnKF analyses to extend the observations presented by S14 of internal RFD momentum surges occurring in a supercell sampled during the second Verification of the Origin of Rotation in Tornadoes Experiment (VORTEX2; Wurman et al. 2012) west of Dumas, Texas, on 18 May 2010. S14 documented the evolution of four internal RFD momentum surges over a 15-min period, concurrent with the development, intensification, and decay of a low-level¹ mesocyclone. The final three observed surges developed across the western periphery of the low-level mesocyclone in a region of inferred downward-directed perturbation pressure gradient forcing and were speculated to be the surface manifestation of an occlusion downdraft (Klemp and Rotunno 1983; Wicker and Wilhelmson 1995; Wakimoto et al. 1998; Adlerman et al. 1999; Wakimoto and Cai 2000). The EnKF experiments considered herein are produced using independent observations from those examined by S14 and are analyzed to address two primary questions:

- What are the dominant forcing mechanisms for the development of internal RFD momentum surges in the Dumas supercell?
- Where is the source region for air parcels within the near-surface RFD surges?

A detailed description of the available data, numerical model, and EnKF technique are presented in section 2.

¹ Distinctions between “near surface” and “low level” in this study follow the convention of S14, with “near surface” representing the lowest elevation angle or available model level, generally below 100 m aloft, and “low level” indicating approximately the lowest 1 km of the atmosphere.

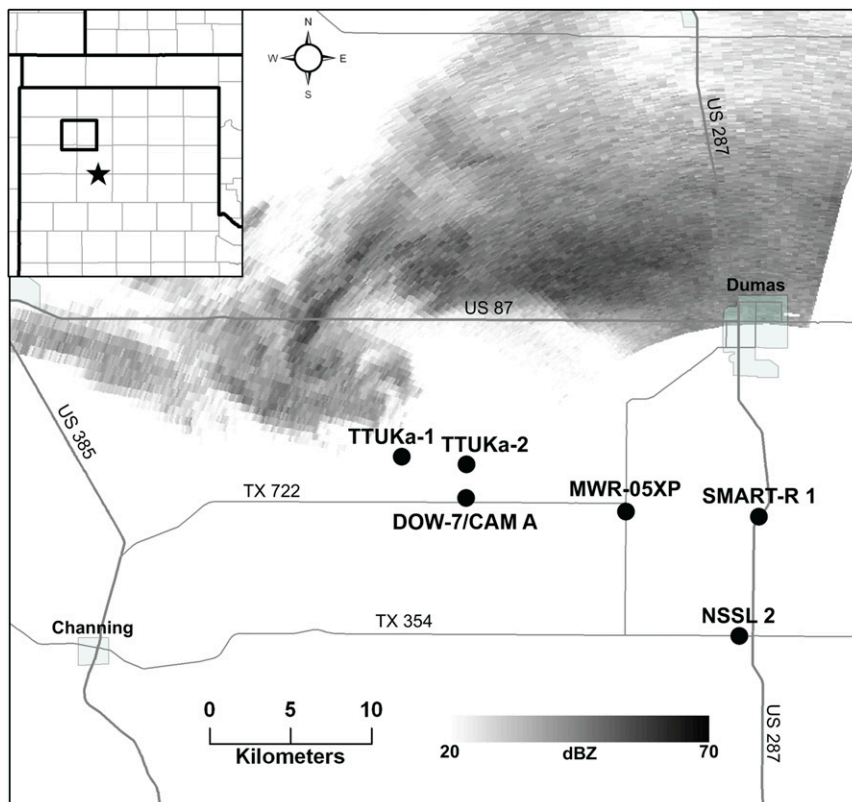


FIG. 1. Overview of VORTEX2 deployment locations during the period of interest, reprinted from S14 for convenience. SMART-R 0.8° elevation radar reflectivity values greater than 20 dBZ at 2257:13 UTC are overlain. The inset displays the position of the figure (bold box) relative to the Texas Panhandle and Amarillo, TX (star).

Analyses of the EnKF retrievals of the Dumas supercell and comparison to independent observations are provided in section 3, with analysis of RFD surge forcing mechanisms and air parcel source regions following in section 4. Conclusions and recommendations for future research are provided in section 5.

2. Analysis methods

a. Case overview and dataset description

This study focuses on a brief period between 2250 and 2300 UTC, which encompasses the intensification of both a nontornadic low-level mesocyclone and RFD surge following a series of mergers between the Dumas supercell and nonsupercellular convection.² The Dumas supercell was well sampled by VORTEX2 assets during this period and data collection included observations

from five mobile Doppler radars (Fig. 1). S14 primarily analyzed data from three of these radars: near-surface dual-Doppler data collected by two Texas Tech University Ka-band mobile Doppler radars (TTUKa; Weiss et al. 2009; Hirth et al. 2012) and single-Doppler, volumetric data collected at X-band by the phased-array MWR-05XP (Bluestein et al. 2010). EnKF analyses herein are produced by assimilating volumetric radial velocity data collected by a Doppler on Wheels (DOW; Wurman et al. 1997) and Shared Mobile Atmospheric Research and Teaching Radar (SMART-R; Biggerstaff et al. 2005), as well as radial velocity and radar reflectivity data collected by the KAMA (Amarillo, Texas) WSR-88D (Figs. 1 and 2).

Prior to assimilation, mobile radar data were quality assured in the same manner as in S14. Data were rotated to the proper orientation, thresholded on radar reflectivity to remove low-power returns, then manually dealiased and edited to remove regions of velocity folding and ground clutter. A simple radar reflectivity threshold of 20 dBZ was applied to KAMA data, and automated dealiasing was performed within the data

² A complete description of the evolution and environment of the Dumas supercell is available in S14.

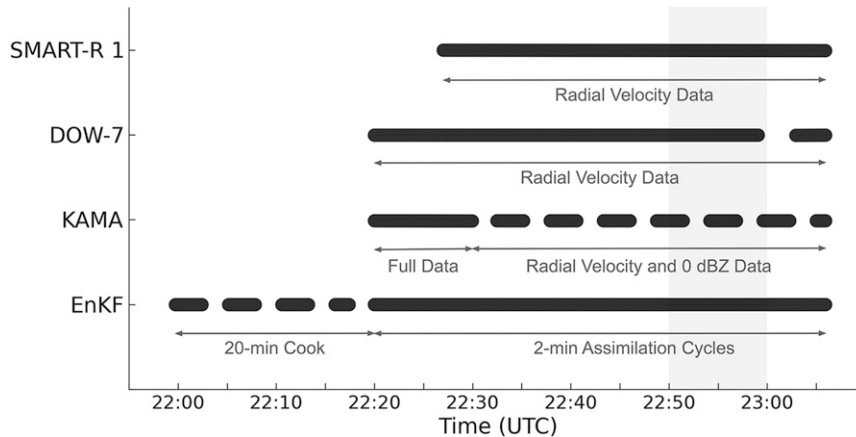


FIG. 2. Timeline of the EnKF experiment and availability of SMART-R, DOW, and KAMA WSR-88D data sources. The initial 20-min “cook” period of the EnKF experiment, where perturbations are allowed to grow in the ensemble prior to data assimilation, is indicated by a dashed line. KAMA data are separated into periods where both radial velocity and radar reflectivity observations (solid) and only radial velocity and zero-value radar reflectivity observations (dashed) are assimilated. Only radial velocity observations are assimilated from the SMART-R and DOW platforms. Light shading indicates the period of interest for this study.

assimilation system. Following quality assurance, data from individual radar scans were objectively analyzed to a Cartesian grid on the original conical surface of the scan (e.g., [Dowell et al. 2004](#); [Dowell and Wicker 2009](#)). A two-pass Barnes objective analysis scheme ([Majcen et al. 2008](#)) was applied to the mobile radar data and a Cressman scheme was applied to the KAMA data ([Table 1](#)), with extrapolation of radar data permitted provided at least three observations with a combined weight of at least 0.1 were available. The use of the two-pass Barnes scheme, as well as smaller grid spacing, for objectively analyzed mobile radar data ([Table 1](#)) is intended to minimize smoothing and preserve the representation of small-scale phenomena such as internal RFD momentum surges. KAMA data are assimilated to supplement the higher-resolution radial velocity data from the two mobile Doppler radars, define regions where noise is added ([Dowell and Wicker 2009](#)), and suppress spurious convection ([Tong and Xue 2005](#)). As the retrieved wind field of the Dumas supercell is primarily determined by radial velocity data from the DOW and SMART-R mobile Doppler radars, coarser grid spacing and a Cressman

analysis scheme are applied to the KAMA data to reduce computational expense.

b. Numerical model configuration

An initial estimate of the atmospheric state of the Dumas supercell is produced using an ensemble of numerical simulations from the National Severe Storms Laboratory Collaborative Model for Multiscale Atmospheric Simulation (NCOMMAS; [Wicker and Skamarock 2002](#); [Coniglio et al. 2006](#)). NCOMMAS is a non-hydrostatic, compressible cloud model that simulates convection in a homogeneous environment without surface fluxes or radiative transfer. The model integrates values of the zonal wind u , meridional wind v , vertical wind w , Exner function π , mixing coefficient K_m , potential temperature θ , and a number of mixing ratios dependent on the microphysical parameterization employed. Each simulation uses the time-splitting integration method of [Wicker and Skamarock \(2002\)](#) with large (small) time steps of 2 (0.33) s. A stationary simulation domain extending $100 \text{ km} \times 100 \text{ km} \times 20 \text{ km}$ is employed, with uniform 500-m horizontal grid spacing and a stretched vertical grid of 80 levels with minimum

TABLE 1. Summary of objective analysis parameters for assimilated radar data with Δ representing the horizontal and vertical grid spacing in km, κ is the Barnes smoothing parameter, γ is the second-pass convergence parameter, and the Cressman radius of influence is in km.

Radar(s)	Domain (x - y)(km \times km)	Δ (km)	Analysis method	κ (γ)	Radius of influence (km)
SMART-R-1	100 \times 100	1	Barnes	3.063 (0.3)	
DOW-7	100 \times 100	1	Barnes	0.298 (0.3)	
KAMA	100 \times 100	2	Cressman		2

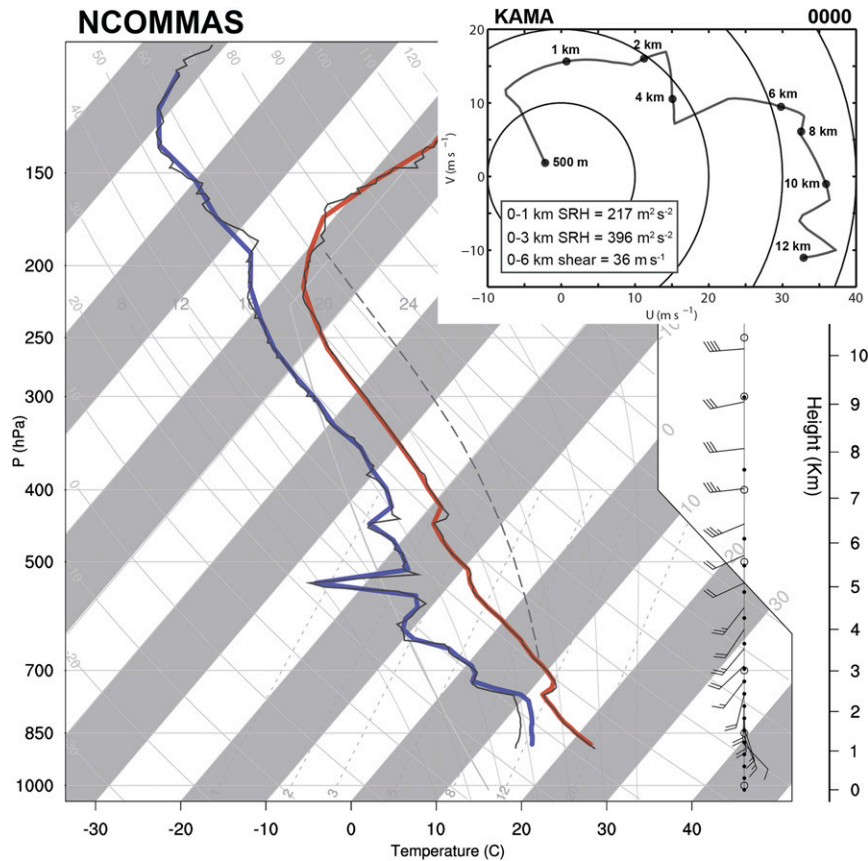


FIG. 3. Skew T -log p diagram of the input sounding for NCOMMAS simulations, with the environmental virtual temperature plotted in red, dewpoint temperature in blue, and a surface parcel trajectory in dashed gray. The unmodified 2152 UTC NSSL-2 sounding is underlaid in gray for reference. Ground-relative hodograph of the base-state environmental wind profile provided by the 0000 UTC KAMA sounding is included as an inset at the top right.

(maximum) spacing of 100 (700) m at the bottom (top) of the domain. The two-moment version of the Ziegler variable density scheme (ZVD; Ziegler 1985; Mansell et al. 2010) is used for the microphysical parameterization.

The initial thermodynamic environment for each simulation is homogeneous and based on a mobile sounding collected by VORTEX2 (Parker 2014) at 2152 UTC approximately 40 km to the east-southeast of the developing Dumas supercell (Fig. 3), then modified by adjusting the boundary layer potential temperature and dewpoint temperature toward mobile mesonet observations collected ahead of the RFD of the storm during the period of interest (S14). The initial wind profile for each ensemble member is based on the 0000 UTC 19 May 2010 KAMA sounding (Fig. 2). The KAMA wind profile was used in place of the VORTEX2 sounding as it exhibits far less small-scale variation with height (S14, their Fig. 3b), which may result in large-scale changes to the environmental hodograph

when interpolated to the NCOMMAS vertical grid. Convection is initiated in each member by random placement of $7.5 \text{ km} \times 7.5 \text{ km} \times 1.5 \text{ km}$, sinusoidally varying thermal bubbles with a maximum perturbation potential temperature of 4 K within the domain. Bubble placement is limited to regions where KAMA 0.5° radar reflectivity exceeded 30 dBZ at the time of model initialization.

Choices in numerical model configuration unavoidably introduce errors into resulting analyses. These model errors arise from many sources, including the use of an idealized framework with a homogeneous initial state, as well as from the grid spacing and physical parameterizations employed. Despite these limitations, similar frameworks have been previously used to retrieve representative three-dimensional kinematic and thermodynamic fields within supercells (e.g., Marquis et al. 2012; Tanamachi et al. 2013; Marquis et al. 2014; Tanamachi et al. 2015). Additionally, it is noted that EnKF kinematic analyses have been found

to be relatively insensitive to small errors in the initial environment (Potvin and Wicker 2012; Potvin et al. 2013) and the use of different microphysical parameterizations (Marquis et al. 2014) when radial velocity data from multiple mobile Doppler radars are assimilated.

c. EnKF configuration

The NCOMMAS EnKF system used in this study employs an ensemble square root filter (Whitaker and Hamill 2002). The ensemble square root filter is used to serially assimilate Doppler radar observations within 2-min windows in order to update initial state and background error covariance estimates provided by an ensemble of 48 NCOMMAS simulations. Observations are weighted in space according to the correlation function of Gaspari and Cohn (1999), with weights decreasing to 0 at horizontal (vertical) cutoff radii of 6 (3) km. Radial velocity observations are allowed to update each model state variable except π and K_m , which have been found to be minimally impacted during assimilation (Tong and Xue 2005; Dowell and Wicker 2009). Uncalibrated radar reflectivity values from the DOW and SMART-R platforms are not assimilated and nonzero radar reflectivity data from KAMA are prevented from updating θ to limit their impact on the near-surface cold pool (Dowell et al. 2011). Furthermore, nonzero radar reflectivity data from KAMA are only assimilated during the first five assimilation cycles (up to 2230 UTC; Fig. 2) in order to aid in the development of convection in ensemble members and provide boundaries for the placement of additional thermal bubbles following the first assimilation cycle at 2220 UTC (Fig. 2). Following 2230 UTC, assimilation of positive KAMA radar reflectivity data is terminated to avoid negatively impacting the accuracy of the three-dimensional wind analyses (Potvin and Wicker 2012; Potvin et al. 2013). Regions of missing data are assimilated as 0-dBZ observations throughout the experiment in order to suppress spurious convection (Tong and Xue 2005).

Uncertainty in the initial environment, used to provide the background-error covariances required by the ensemble Kalman filter, is represented by perturbing the environmental wind profile of each member (Aksoy et al. 2009). Sinusoidal perturbations with standard deviations that increase linearly with height from 2 to 6 m s^{-1} are added to the u and v components of the wind similarly to Potvin et al. (2013). Following initialization, ensemble spread within the Dumas supercell is maintained through the additive-noise technique of Dowell and Wicker (2009). Smoothed Gaussian perturbations with length scales of 4 (2) km in the horizontal (vertical)

and amplitudes of 1 m s^{-1} (0.5 K) are added to the u and v (θ and dewpoint temperature) fields in regions with greater than 10-dBZ observed radar reflectivity following each assimilation cycle. The magnitudes and length scales of the additive-noise perturbations were chosen through trial and error and are similar to those used in prior studies (e.g., Dowell and Wicker 2009; Marquis et al. 2012; Potvin and Wicker 2012; Potvin et al. 2013).

The 48-member ensemble is initiated at 2200 UTC and run for 20 min prior to the first assimilation cycle (Fig. 2) in order to allow realistic covariances to develop within the ensemble (Snyder and Zhang 2003; Dowell et al. 2004). Beginning at 2220 UTC, radial velocity data are assimilated at 2-min intervals until 2310 UTC (Figs. 2 and 4). Following approximately seven assimilation cycles a relatively stable retrieval of the observed wind field of the Dumas supercell is reached in terms of the root-mean-square of the innovation (RMSI), with forecast(analysis) radial velocity RMSI values within $2\text{--}3$ ($1\text{--}2$) m s^{-1} (Fig. 4). Examination of the ratio of the sum of the variance of the observation error and model observation priors to the innovation variance, known as the consistency ratio³ (Dowell et al. 2004), reveals values below the ideal value of 1.0 during the majority of the experiment and decreasing values with time, indicative of an under-dispersive analysis. However, calculated consistency ratios vary with height and values in the lowest 2 km above ground level (AGL) remain between roughly 0.7 and 1.3 (not shown), suggesting that an appropriate amount of ensemble spread is present in the low levels of the Dumas EnKF analyses. A brief period where DOW data are unavailable between 2259 and 2303 UTC results in an abrupt increase in RMSI following the 2300 UTC assimilation cycle (Fig. 4) and rapid changes in the ensemble mean analyses following 2300 UTC (not shown); as a result, only analyses up to 2300 UTC are considered in this study.

3. EnKF analyses of the Dumas supercell

a. Storm evolution

At 2250 UTC in the ensemble mean EnKF analyses⁴, an occluded, two-celled, low-level mesocyclone (e.g., Rotunno 1984; Wakimoto and Liu 1998; Trapp 2000) is apparent (Fig. 5a). The maximum low-level vertical vorticity in the western portion of the mesocyclone occurs

³ A thorough description of the observation-space diagnostics used in this study can be found in Dowell and Wicker (2009).

⁴ The ensemble mean is utilized for each analysis herein. Comparison of analyses produced by individual members revealed small variations that did not impact interpretation of the results (not shown).

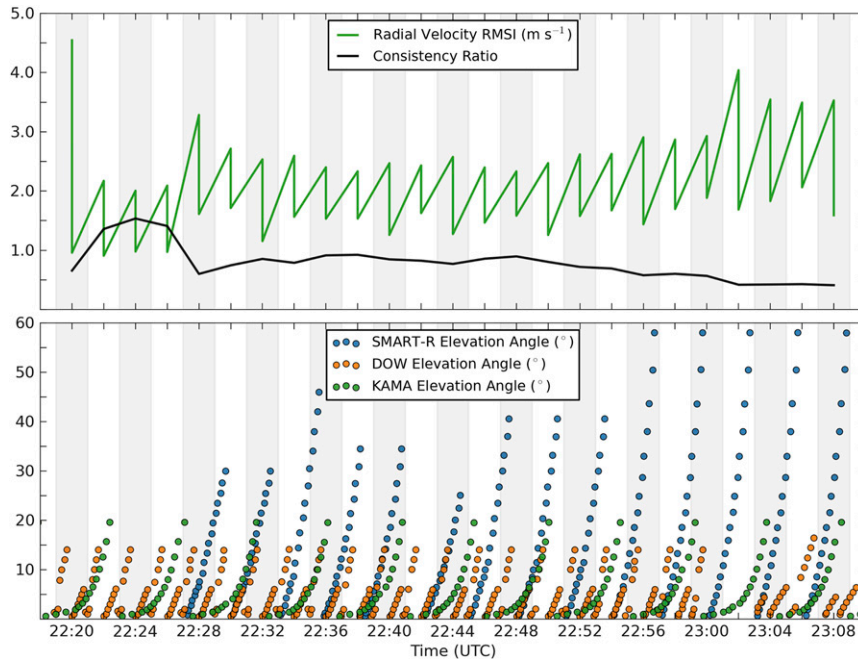


FIG. 4. Time series of (top) radial velocity root-mean-square error innovation (RMSI; m s^{-1}) and consistency ratio and (bottom) elevation angles ($^{\circ}$) of SMART-R, DOW, and KAMA data assimilated each cycle. Every second assimilation window is shaded gray and both the forecast and analysis RMSI are plotted in the top panel.

above a region of enhanced convergence and a weaker mesoanticyclone is apparent south of the maximum (Fig. 5a). Both counter-rotating vorticity maxima trail the strong near-surface convergence in the RFD gust front and weaker convergence along a forward-flank gust front extending north-northeastward from the low-level mesocyclone (Fig. 5a). A broad region of near-surface wind speed greater than 18 m s^{-1} is present in the RFD across the western and southern periphery of the low-level mesocyclone (Fig. 5b). Though the near-surface wind speed maximum is located between the counter-rotating vorticity maxima and trails the leading edge of the RFD gust front, similar wind speeds and divergence are found ahead of the maximum through the RFD gust front, indicating a lack of a cohesive internal RFD surge at this time. A modest near-surface cold pool is present, as seen in the perturbation virtual potential temperature⁵ field, with

⁵ Perturbation virtual potential temperature values include the effects of liquid water and ice and are calculated with the following formula:

$$\theta_v = \theta(1 + 0.61q_v - q_c),$$

where θ_v is the virtual potential temperature, q_v is the water vapor mixing ratio, and q_c is the sum of the cloud water, rain, ice, snow, graupel, and hail mixing ratios calculated by the ZVD scheme. The θ_v of the initial environment is used as the base state.

values of roughly -2 K in the RFD and maximum deficits of 6 K northwest of the low-level mesocyclone (Fig. 5c). These simulated thermodynamic deficits are similar in magnitude and location to in situ observations from a mobile mesonet (Straka et al. 1996; Waugh and Fredrickson 2010) at a similar time (S14) and StickNet (Schroeder and Weiss 2008) approximately 30 min following the period of interest (Weiss et al. 2015).

The two-celled low-level mesocyclone persists through the following two analyses: with the western vorticity maximum intensifying and merging with a secondary vorticity maximum rotating around the northern periphery of the mesocyclone (Figs. 5d,g). Convergence underneath the western vorticity maximum merges with expanding convergence underneath the low-level mesoanticyclone by 2254 UTC, resulting in a contiguous region of convergence within the broadscale RFD bridging the counter-rotating vortices (Fig. 5g). The development of this convergence zone is coincident with intensifying downward motion, divergence, and horizontal wind speed trailing the convergence zone and a deceleration of the wind speed along and immediately ahead of the convergence zone (Figs. 5d–i). This evolution results in the development of a local maximum in horizontal momentum within the broadscale RFD located between

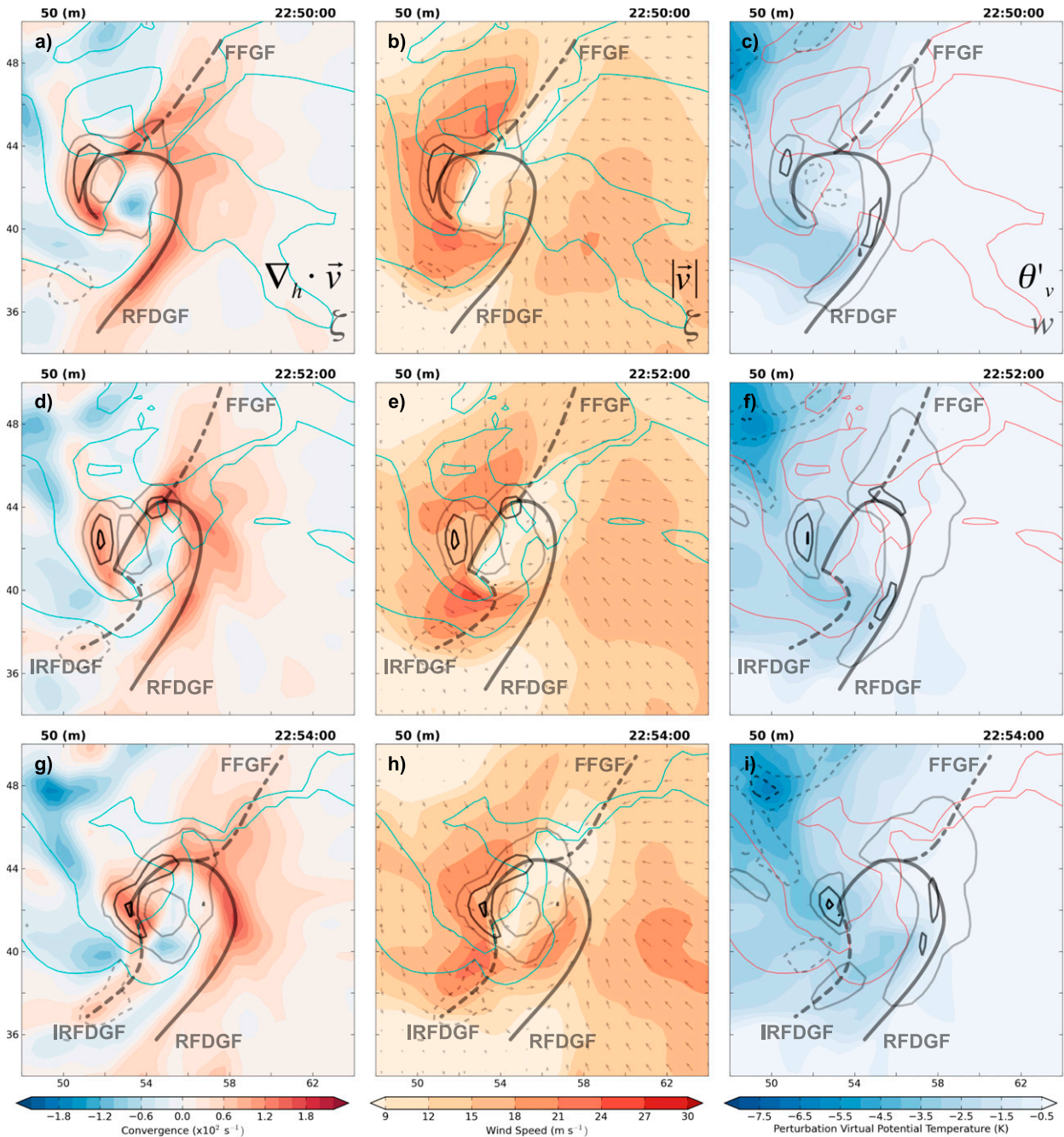


FIG. 5. Ensemble mean analyses at the lowest model level (50 m AGL) of (a),(d),(g) convergence (s^{-1}); (b),(e),(h) wind speed with every other wind vector plotted (m s^{-1}); and (c),(f),(i) perturbation virtual potential temperature (K) at (a)–(c) 2250, (d)–(f) 2252, and (g)–(i) 2254 UTC. Vertical vorticity (vertical velocity) at 600 m AGL is contoured in grayscale every 0.0075 s^{-1} (3 m s^{-1}) over plots of convergence and wind speed (perturbation virtual potential temperature) with anticyclonic vorticity (downward velocity) indicated by dashed contours. Positions of the forward-flank gust front (FFGF), RFD gust front (RFDGF), and internal RFD surge gust front (IRFDGF) at the lowest grid level are subjectively analyzed based on the convergence and wind speed fields and annotated with thick stippled, solid, and dashed gray lines, respectively. Simulated radar reflectivity contours of 20, 40, and 60 dBZ are plotted in cyan on convergence and wind speed plots, and red for perturbation virtual potential temperature plots. Axes are labeled in km from the southwest corner of the simulation domain and shaded (contoured) values plotted in each column are provided in the bottom-right corner of the top row of plots.

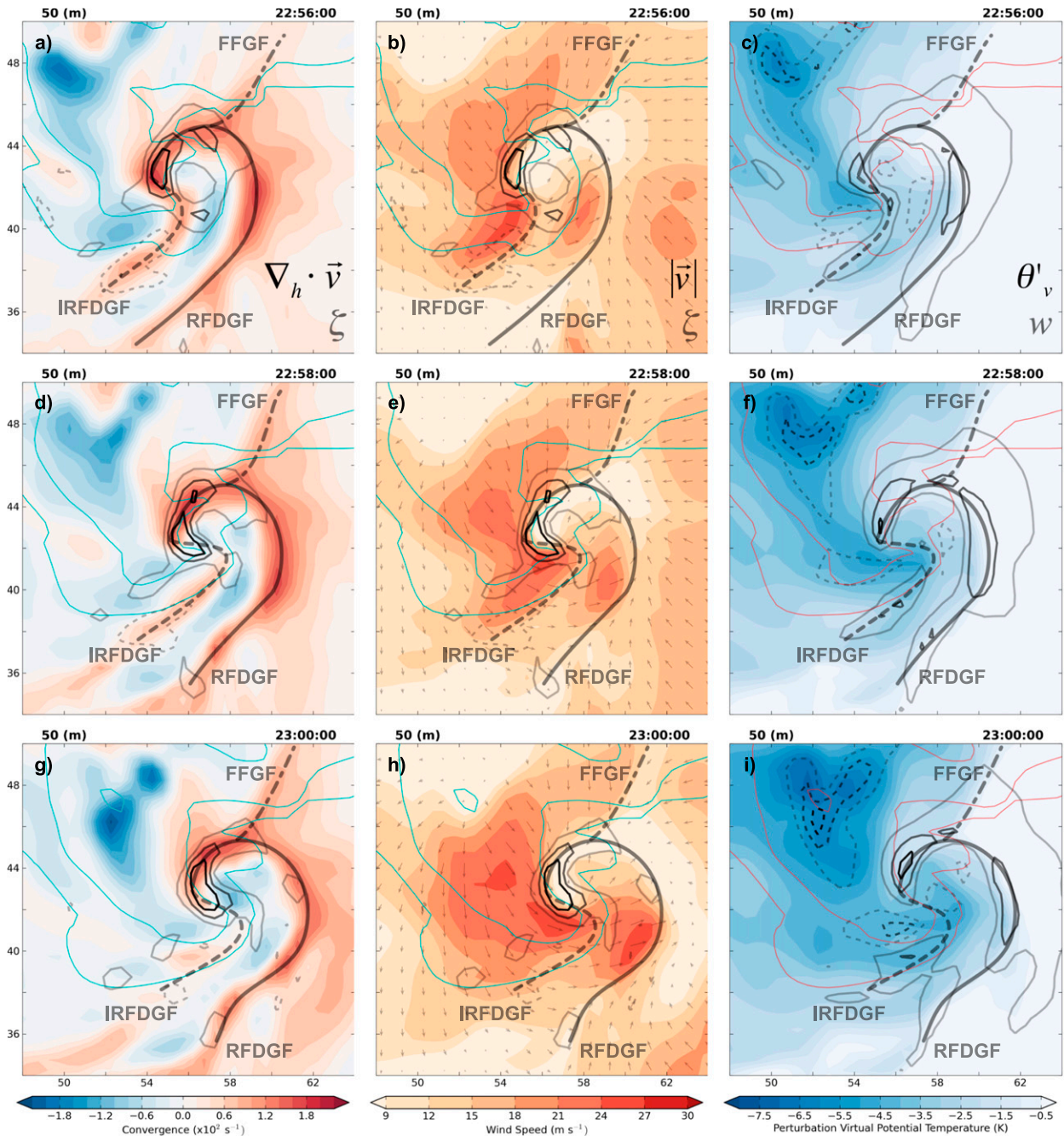


FIG. 6. As in Fig. 5, but for (a)–(c) 2256, (d)–(f) 2258, and (g)–(i) 2300 UTC.

counter-rotating low-level vorticity maxima and bounded by convergence along its leading edge, indicative of an internal RFD momentum surge. A southeastward expansion of the minimum perturbation θ_v also occurs during this period (Figs. 5f,i) such that maximum deficits of 3.5 K are present across the northern portions of the RFD surge, with smaller deficits ahead of the surge. The 1–2-K drop in virtual potential temperature in the RFD

surge compared to the broadscale RFD is similar to mobile mesonet observations during the same time period (S14).

The internal RFD surge and associated gust front are clearly apparent in the 2256 UTC analyses (Figs. 6a–c). Maximum wind speeds within the surge are greater than 25 m s^{-1} with an abrupt deceleration to below 15 m s^{-1} ahead of the RFD surge gust front (Fig. 6b).

Convergence along the RFD surge gust front has intensified with upward low-level vertical velocities greater than 3 m s^{-1} present along the entirety of the gust front at 600 m aloft (Figs. 6a,c). Additionally, the local maximum in divergence and downward vertical velocity trailing the RFD surge gust front has expanded from 2 min prior (Figs. 5g,i). The low-level mesocyclone now clearly exhibits a multiple-vortex structure (Rotunno 1984; Trapp 2000; Wurman and Kosiba 2013) with the strongest vorticity maximum residing above the intersection of the occluded RFD gust front and internal RFD surge gust front (Fig. 6a). The low-level mesoanticyclone has also intensified and expanded above the convergence along the southern portions of the RFD surge gust front. In addition to an east–west buoyancy gradient across the RFD surge gust front, a north–south buoyancy gradient is apparent within the internal RFD surge, where a local maximum in perturbation virtual potential temperature deficit of approximately 4 K across the northern portions of the surge decreases to about a 2-K deficit over the southern extent (Fig. 6c).

Convergence and upward vertical velocity along the apex of the internal RFD surge decrease during the final two analyses, resulting in a break in the RFD surge gust front (Figs. 6e,h). However, the RFD surge is still apparent as a distinct maximum in horizontal momentum with convergence bounding its southern extent. This break in convergence across the apex of the surge is similar to observations in several previous dual-Doppler studies of RFD surges (Wurman et al. 2007; Marquis et al. 2008; Wurman et al. 2010; Marquis et al. 2012; Kosiba et al. 2013; S14). The two-celled structure of the low-level mesocyclone breaks down by 2300 UTC with the vorticity maximum above the intersection of the RFD and RFD surge gust fronts continuing to intensify (Figs. 6d,g). In contrast, the low-level mesoanticyclone weakens considerably during this period coincident with a reduction of convergence along the southern extent of the internal RFD surge gust front (Figs. 6d,g). The near-surface wind field throughout the RFD intensifies during this period and θ_v deficits greater than 3 K expand through the southern portions of the RFD surge and broadscale RFD (Figs. 6e–i).

b. Comparison to observations

The wealth of mobile Doppler radar data available during the period of interest allows the representativeness of the EnKF-retrieved wind field to be qualitatively assessed through comparison with independent observations. TTUKa-2 mobile Doppler radial velocity data collected at a 0.0° elevation angle

have been objectively analyzed using the same methodology as in S14, except to a more coarse, 500-m horizontal grid in order to facilitate comparison to the near-surface ensemble mean wind speed. Comparison between the two fields reveals similar placement, extent, and evolution of the internal RFD momentum surge (Fig. 7), with spatial differences in the location of the RFD surge wind maximum and estimated positions of the primary and RFD surge gust fronts typically less than 1 km throughout the period of interest. A second internal RFD surge, which was first observed in TTUKa data at approximately 2259 UTC (S14, see their supplemental material), is smoothed out of data interpolated to the coarse 500-m horizontal grid (Fig. 7f) and is manifest as a broadening of inbound radial velocities greater than 20 m s^{-1} along the western periphery of the mesocyclone. A similar intensification of the near-surface wind field to the west and northwest of the low-level mesocyclone is present in the 2300 UTC EnKF analysis (Fig. 7c). One difference between the fields is that consistently higher maximum wind speeds are observed in the TTUKa radial velocity data, which are up to 5 m s^{-1} greater than EnKF wind maxima. The majority of this discrepancy is likely attributable to added smoothing of radial velocity data assimilated by the EnKF, which are analyzed to a 1-km horizontal grid using a coarser first-pass smoothing parameter than the TTUKa data. Additionally, the parameterization of turbulent mixing in NCOMMAS and gridpoint averaging to calculate the ensemble mean wind field likely also contribute to differences in the observed and simulated near-surface wind speed.

Assessment of the EnKF representation of the development of the low-level mesocyclone documented by S14 is more difficult owing to a lack of coordinated, volumetric dual-Doppler observations across the mesocyclone of the Dumas supercell (Fig. 1). However, a qualitative comparison can be undertaken between EnKF vertical vorticity and azimuthal wind shear values calculated from MWR-05XP radial velocity data, provided several caveats are considered. The first caveat is that using azimuthal wind shear as a proxy for vertical vorticity requires an assumption of solid-body rotation, which breaks down in regions of strong horizontal deformation such as those found within the low levels of the Dumas supercell. Additionally, the magnitude of azimuthal wind shear is dependent on both properties of the radar data specific to individual radars such as beamwidth and range, as well as properties of the objective analysis scheme employed. Finally, the lack of a hydraulic leveling system in the MWR-05XP during VORTEX2 results in spatial errors in the data

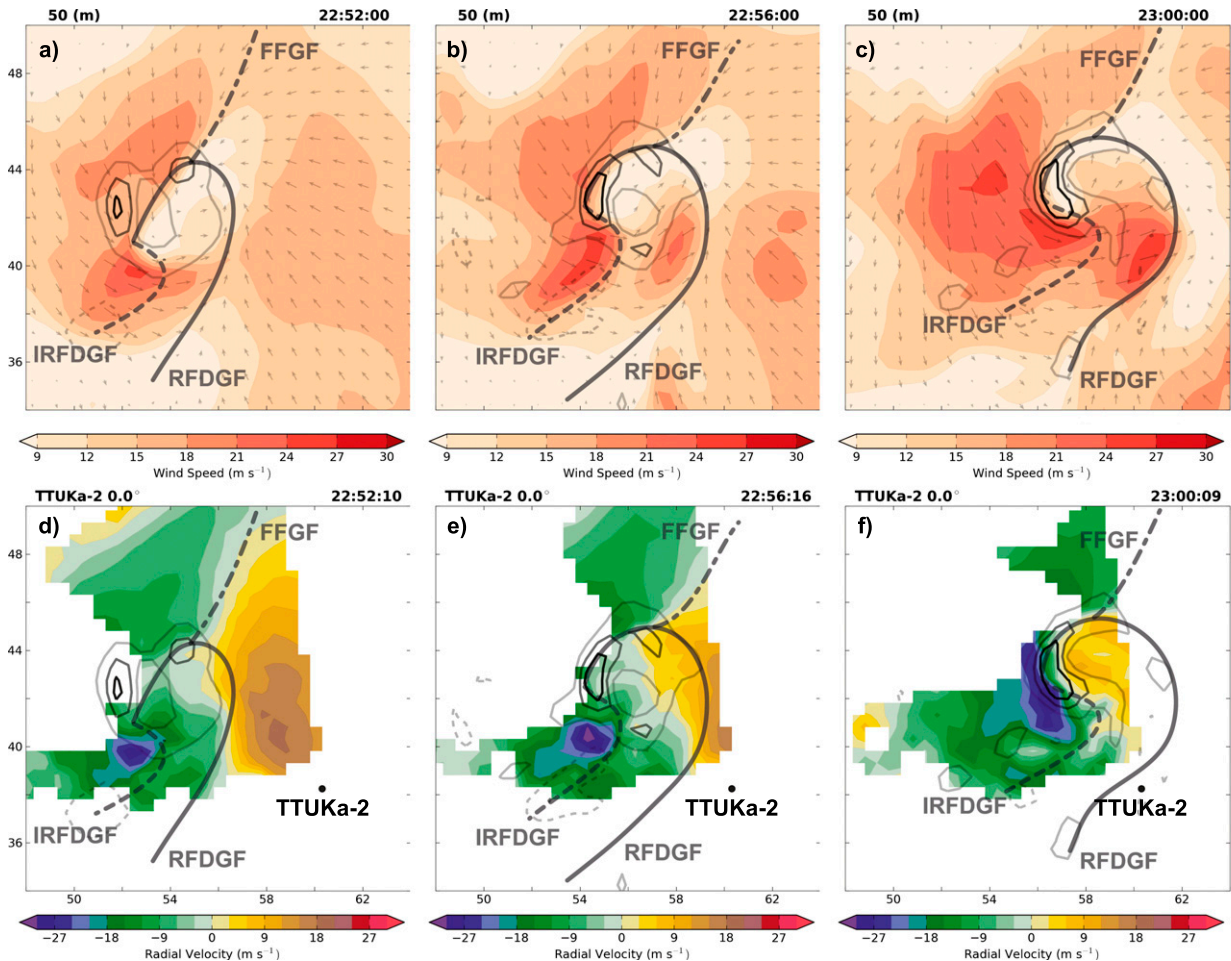


FIG. 7. Values of (a)–(c) ensemble mean near-surface wind speed (m s^{-1}) and (d)–(f) TTUKa 0.0° elevation angle radial velocity (m s^{-1}) data objectively analyzed to a 500-m horizontal grid. Grayscale contours of 600-m ensemble mean vertical vorticity and subjectively analyzed gust front positions are as in Fig. 5 and plotted over both wind speed and TTUKa-2 data in order to provide spatial reference points. The location of TTUKa-2 is indicated by a black dot.

collected (French et al. 2013). Though horizontal displacement errors are expected to be less than 100 m for the Dumas deployment (see Table A1 in S14), vertical displacement errors of up to 1 km and the strong south–north tilt of the Dumas low-level mesocyclone (S14; Figs. 7 and 14) make direct comparison at a specific level difficult.

Despite these limitations, single-Doppler azimuthal wind shear has been found to be qualitatively similar to vertical vorticity values calculated using dual-Doppler data (Markowski et al. 2012a; S14); suggesting that a broad comparison between representations of the low-level mesocyclone in MWR-05XP and the EnKF ensemble mean can be undertaken (Fig. 8). A generally similar appearance and evolution to the low-level mesocyclone is apparent in MWR-05XP azimuthal wind shear data objectively analyzed to a 500-m horizontal grid and EnKF vertical vorticity data, though with some temporal and spatial variation.

Primary differences include a consistent local vertical vorticity maximum approximately 1 km aloft in the EnKF retrievals that is not apparent in the MWR-05XP data and earlier upward development of the low-level mesocyclone in the EnKF retrievals (Figs. 8c,d). Despite these differences, the general evolution of the low-level mesocyclone remains similar in both analyses, with a lack of rotation at the lowest levels early in the period of interest (Figs. 8a,b), followed by intensification and upward growth of a low-level mesocyclone distinct from the midlevel mesocyclone (Figs. 8c–f). The positions of the low-level mesocyclone, attendant mesoanticyclone, and lower portions of the midlevel mesocyclone are similar throughout the analysis period, as is the northward tilt to the low-level mesocyclone. A more upright and intense mid- to upper-level mesocyclone is present in the EnKF analyses than MWR-05XP data from approximately 5 km upward (Fig. 8), which is likely attributable to the shallow scanning strategy

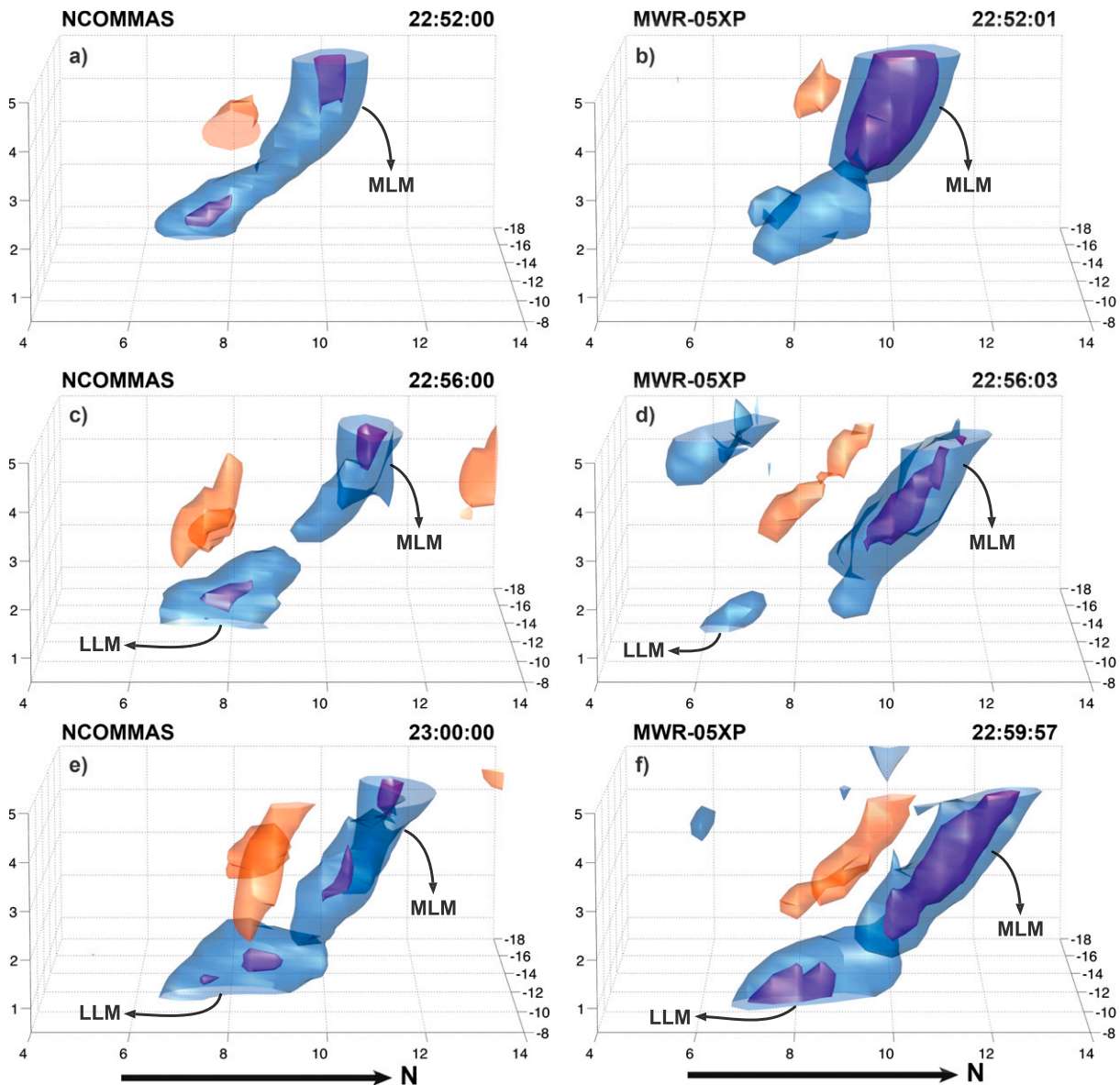


FIG. 8. Three-dimensional isosurfaces of (a),(c),(e) ensemble mean vertical vorticity (s^{-1}) and (b),(d),(f) MWR-05XP azimuthal wind shear (s^{-1}) at approximately (a),(b) 2252; (c),(d) 2256; and (e),(f) 2300 UTC. Cyclonic vertical vorticity (azimuthal wind shear) isosurfaces are plotted at 0.02 and 0.03 ($0.01, 0.015$) s^{-1} in blue and purple, respectively, with an anticyclonic vertical vorticity (azimuthal wind shear) isosurface at -0.02 (-0.01) s^{-1} plotted in orange. The viewing angle is from the east at an elevation of 10° , positions of the low- and midlevel mesocyclones are annotated as “LLM” and “MLM,” respectively, and axes are labeled in km from the location of the MWR-05XP.

employed by the DOW and the resulting lack of observations to constrain the wind analyses at the mid- and upper levels (Potvin and Wicker 2012; Potvin et al. 2013).

4. Forcing and parcel analysis

a. Forcing mechanisms of the internal RFD momentum surge

A significant challenge in using EnKF analyses to diagnose physical processes in supercells is the presence of

large errors in the pressure field of imperfect, compressible models (Tong and Xue 2005), which are likely attributable to the generation of acoustic waves by dynamic imbalances in the analyses (Potvin and Wicker 2013b). Despite these large errors in the EnKF pressure analyses, if the pressure errors do not degrade the three-dimensional depictions of the wind and buoyancy fields provided by the EnKF (Potvin and Wicker 2013b), a diagnostic pressure equation can be solved (e.g., Rotunno and Klemp 1982; Klemp and

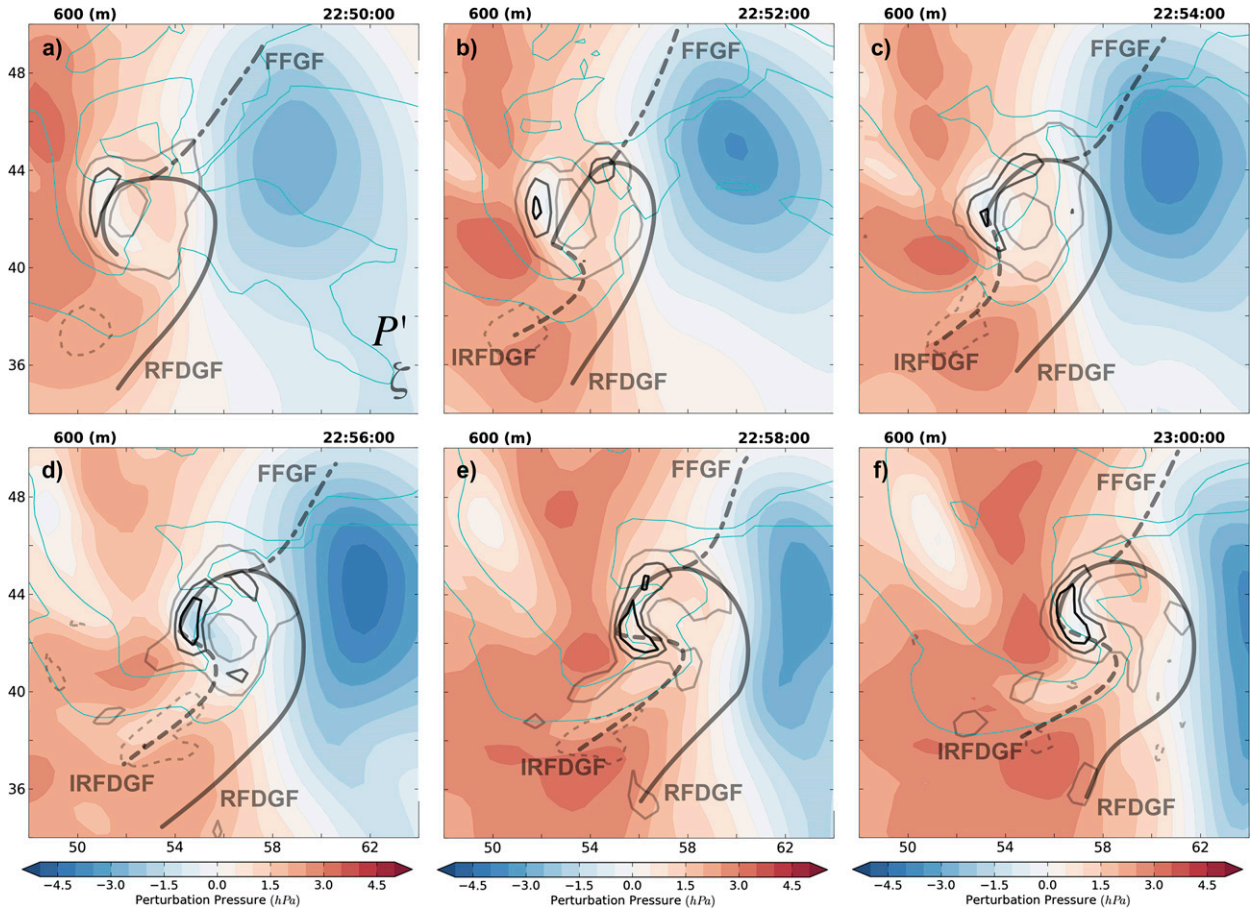


FIG. 9. Retrieved perturbation pressure (hPa) at 600 m AGL at (a) 2250, (b) 2252, (c) 2254, (d) 2256, (e) 2258, and (f) 2300 UTC. Contours of ensemble mean simulated reflectivity (dBZ) and vertical vorticity (s^{-1}), as well as the subjectively analyzed gust front positions, are as in Fig. 5.

Rotunno 1983; Rotunno and Klemp 1985).⁶ The diagnostic pressure equation solved herein is decomposed into three separate Poisson equations following Klemp and Rotunno (1983):

$$\pi' = \pi'_l + \pi'_{nl} + \pi'_B, \quad (1)$$

where subscripts l , nl , and B represent the linear dynamic, nonlinear dynamic, and buoyant components of the total perturbation Exner function (π'). Solving for these individual components allows the inviscid vertical momentum equation to be written as

$$\frac{dw}{dt} = -C_p \bar{\theta}_v \frac{\partial \pi'_{dyn}}{\partial z} - \left(C_p \bar{\theta}_v \frac{\partial \pi'_B}{\partial z} - B \right), \quad (2)$$

⁶ A complete description of the pressure retrieval technique is provided in the appendix.

where dw/dt is the Lagrangian vertical acceleration in meters per second squared, C_p is the heat capacity of air, $\bar{\theta}_v$ is the base-state virtual potential temperature, π'_{dyn} is the sum of the linear and nonlinear dynamic perturbation pressures, and B is the buoyancy, calculated as

$$B = g \left(\frac{\theta'}{\bar{\theta}} + 0.61q'_v - q'_c \right), \quad (3)$$

where g is the gravitational acceleration. Partitioning the diagnostic pressure and vertical momentum equation in this manner allows individual forcing contributions to the development of the internal RFD momentum surge to be examined (Figs. 9–11).

The retrieved low-level perturbation pressure field exhibits a broadly similar structure throughout the period of interest, with a primary minimum in pressure in the storm inflow leading the primary RFD gust front and extending northward into the southern forward-flank

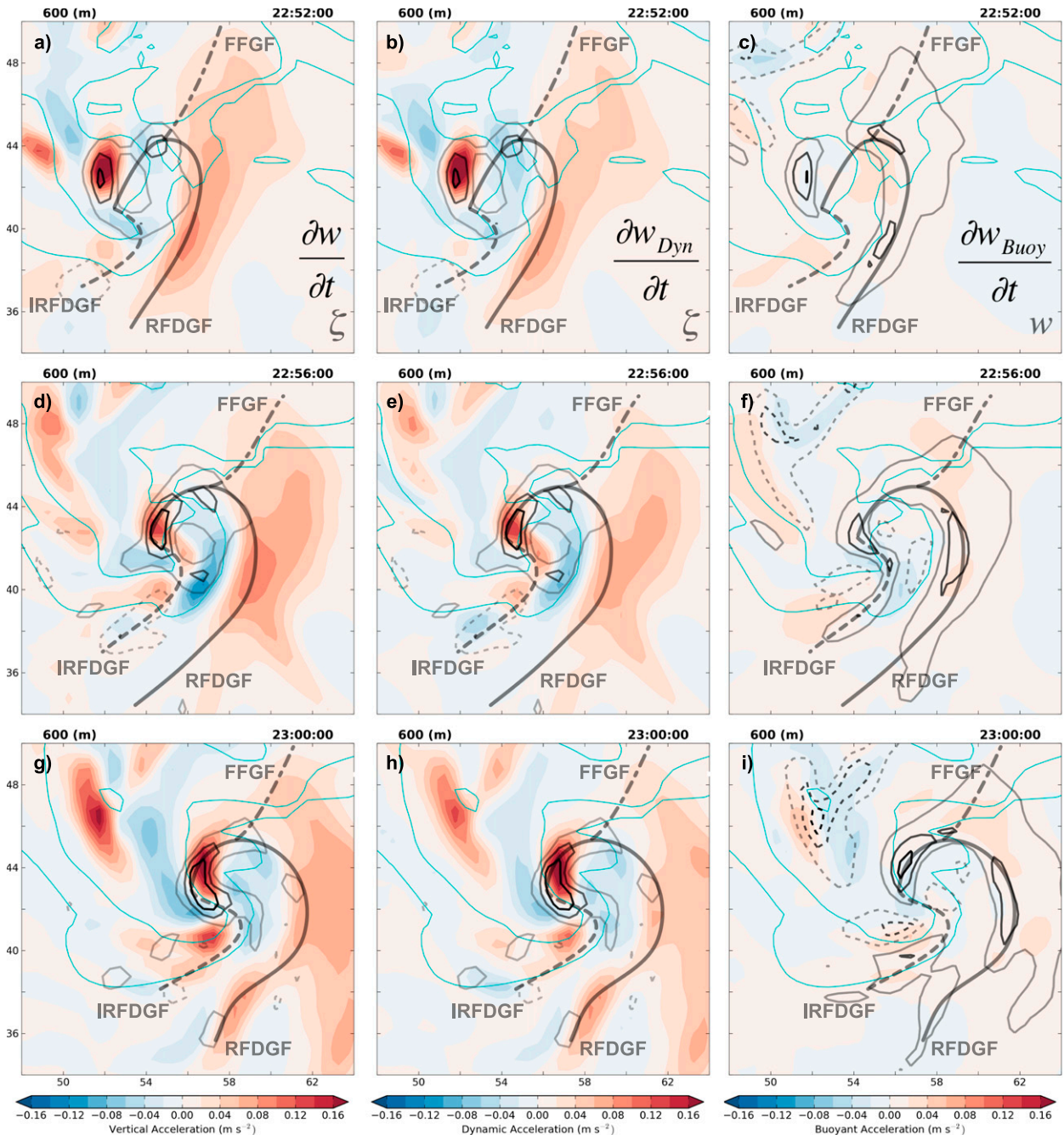


FIG. 10. The 600 m AGL (a),(d),(g) total vertical acceleration (m s^{-2}); (b),(e),(h) dynamic vertical acceleration (m s^{-2}); and (c),(f),(i) buoyant vertical acceleration (m s^{-2}) at (a)–(c) 2252, (d)–(f) 2256, and (g)–(i) 2300 UTC. Ensemble mean (a),(b),(d),(e),(g),(h) vertical vorticity (s^{-1}) and (c),(f),(i) vertical velocity (m s^{-1}), as well as simulated reflectivity (dBZ), subjectively analyzed gust front position, and panel labels are as in Fig. 5.

precipitation shield. This minimum resides between two pressure maxima located within the RFD southwest of the low-level mesocyclone and within the forward-flank precipitation shield downstream of the low-level mesocyclone (Fig. 9). A second, smaller, local pressure minimum is located coincident with the

maximum vertical vorticity values along the western periphery of the low-level mesocyclone. Maximum (minimum) perturbations are roughly 4 (–4) hPa (Fig. 9), and the structure and magnitude of the perturbation pressure field are qualitatively similar to a composite StickNet-observed perturbation pressure field collected

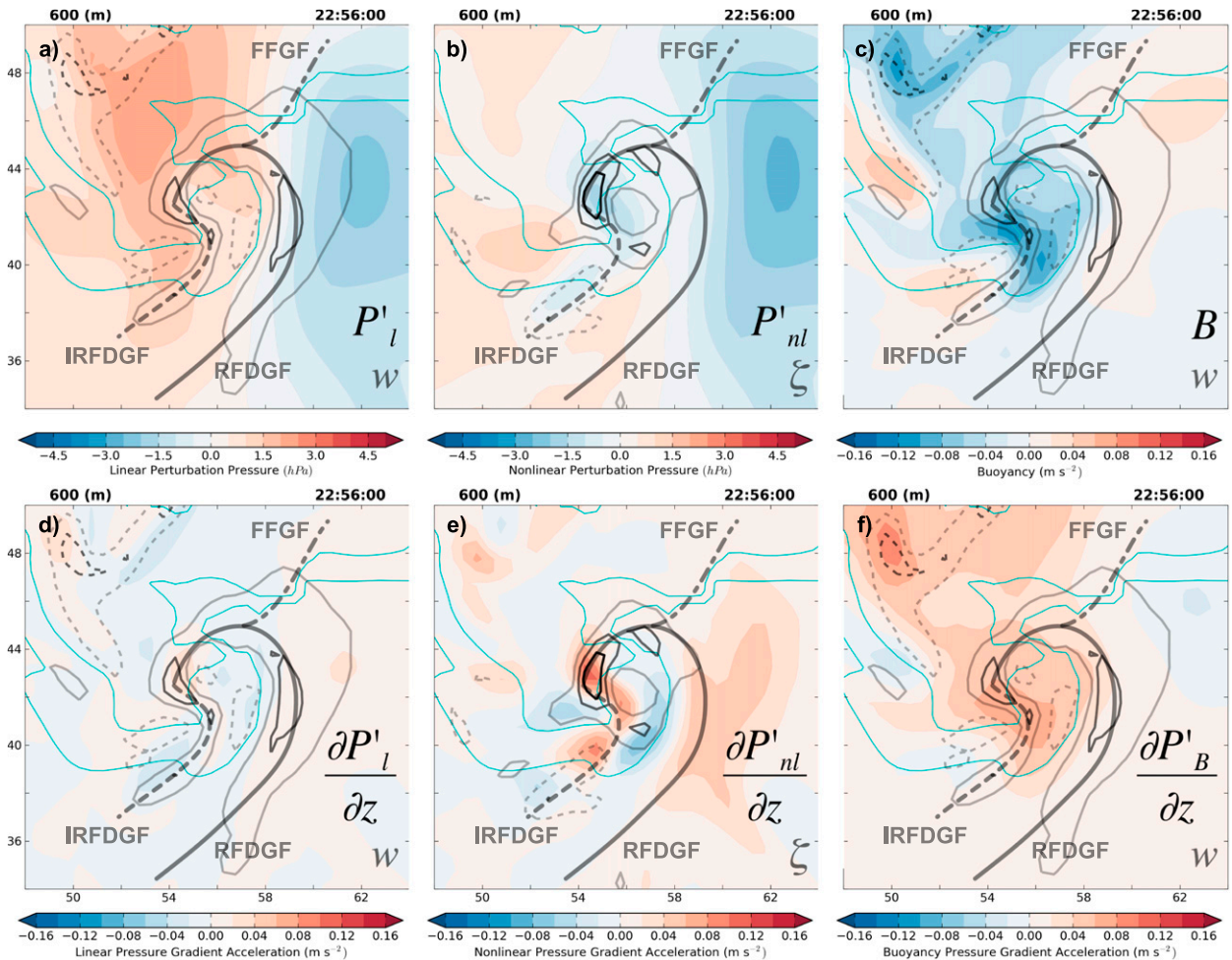


FIG. 11. Contributions to the perturbation pressure (hPa) at 2256 UTC and 600 m AGL from the (a) linear and (b) nonlinear dynamic components with the resulting (d) linear and (e) nonlinear dynamic components of vertical acceleration (m s^{-2}). (c) Thermal buoyancy and (f) buoyant pressure vertical acceleration (m s^{-2}) are plotted. Contours of (a),(b),(d),(e) vertical vorticity (s^{-1}); (c),(f) vertical velocity (m s^{-1}); and simulated reflectivity (dBZ), as well as the subjectively analyzed gust front positions and panel labels are as in Fig. 5.

approximately 30 min following the period of interest (Weiss et al. 2015).⁷

At 2250 UTC, a subtle pressure trough is apparent as a weakness in the region of high perturbation pressure near the low-level mesoanticyclone and extending northeastward to the low-level mesocyclone (Fig. 9a). This trough of locally lower perturbation pressure intensifies over the following two analyses and by 2254 UTC exhibits maximum perturbation pressure differences normal to the

trough axis of greater than 1 hPa, which are maintained through the remainder of the analysis period (Fig. 9). The position of the trough is located above, and slightly trailing, the near-surface internal RFD momentum surge gust front throughout the period (Fig. 9) and is in a similar storm-relative position to a trough identified in dual-Doppler data from the first VORTEX project by Wakimoto and Liu (1998).

The structure of the total vertical acceleration field throughout the period of interest is dominated by the dynamic perturbation pressure gradient forcing (Fig. 10). Low-level buoyancy acceleration is relatively weak as the generally downward acceleration associated with the horizontal gradient of thermal buoyancy within the RFD is counteracted by an upward buoyant perturbation pressure gradient acceleration (Figs. 10c,f). The net buoyant acceleration generally remains negative within

⁷The retrieved pressure field is unresolved to a single, domain-wide constant (e.g., Klemp and Rotunno 1983). The three-dimensional mean perturbation pressure is subtracted from each analysis time in an effort to remove the impact of this constant; however, domain-wide fluctuations in the magnitude of the perturbation pressure field of up to 1 hPa remain apparent between different analysis times (Fig. 9).

the low-level mesocyclone and northern portions of the RFD, with weak upward acceleration farther south in the vicinity of the low-level mesoanticyclone, along the southern portions of the internal RFD surge gust front, and along the primary RFD gust front. The maximum upward acceleration at 2252 UTC is primarily dynamically induced and collocated with the low-level vertical vorticity maximum (Fig. 10). Dynamic upward acceleration increases over the northern portion of the low-level mesoanticyclone, approximately along the internal RFD surge gust front, over the following 6 min such that upward acceleration is present across the entire apex of the RFD surge by 2256 UTC (Fig. 10). A region of downward acceleration, resulting from contributions from both the dynamic and buoyant components of the vertical momentum equation, trails the RFD surge gust front across the southwestern portions of the low-level mesocyclone at 2256 UTC (Figs. 10d–f). This region expands across the apex of the internal RFD surge gust front over the following 4 min as dynamic downward acceleration increases in magnitude and by 2300 UTC has merged with the region of downward acceleration between the two RFD gust fronts leading the low-level vertical vorticity maximum (Figs. 10g–i).

The contribution of linear terms to the perturbation pressure produce high (low) pressure centers upshear (downshear) of the primary updraft, as is expected (Rotunno and Klemp 1982), with a southward extension of the high pressure maximum evident trailing the internal RFD surge gust front (Fig. 11). However, the region of relatively low perturbation pressure trailing the internal RFD surge gust front is primarily a result of the nonlinear-dynamic component of the perturbation pressure, which exhibits a clear trough of low perturbation pressure at 2256 UTC. Similarly, the vertical gradient of the nonlinear perturbation pressure is responsible for the majority of dynamic, and total, vertical acceleration at low levels (Figs. 10d–f and 11e).

The trough of relative low pressure is vertically continuous up to a maximum height of approximately 3 km AGL and is coincident with higher magnitudes of vertical vorticity (Figs. 12 and 13), which would be associated with a local minimum in nonlinear dynamic perturbation pressure (Rotunno and Klemp 1982). The strong south–north tilt of both the low-level mesocyclone and mesoanticyclone results in the low-level mesoanticyclone aloft, from roughly 1 to 3 km AGL, residing above the near-surface low-level mesocyclone (Figs. 12 and 13), which is similar to MWR-05XP azimuthal wind shear observations (S14, their Fig. 14). Two areas of downdraft within the broadscale RFD are observed. One leads the low-level mesocyclone and updraft along the RFD surge gust front (Figs. 6, 12, and 13)

and is within a region of downward-directed vertical perturbation pressure gradient acceleration, similar to prior simulations of an occlusion downdraft (e.g., Klemp and Rotunno 1983; Wicker and Wilhelmson 1995; Adlerman et al. 1999). The second is collocated with the maximum wind speeds within the RFD surge and a region of high perturbation pressure (Figs. 6, 12, and 13) and resembles the structure of a dynamically driven downdraft analyzed by Wakimoto et al. (2003) and an RFD surge in recent simulations by Schenkman et al. (2014a).

Convergent horizontal perturbation pressure gradient accelerations into the trough axis are present throughout the period of interest (Fig. 9). This configuration results in a favorable horizontal perturbation pressure gradient acceleration, which acts to accelerate air parcels wrapping cyclonically around the western periphery of the low-level mesocyclone, followed by an abrupt shift to an adverse horizontal perturbation pressure gradient acceleration as parcels cross the trough axis (Figs. 9 and 12). This process induces the observed acceleration of winds trailing the trough axis, deceleration of winds leading the trough axis, and development of the convergence zone along the trough axis, resulting in the internal RFD momentum surge.

b. Source regions for air parcels within the internal RFD momentum surge

The origins of air parcels within the internal RFD momentum surge are assessed by integrating trajectories within the RFD surge and broadscale RFD backward in time from 2300 to 2250 UTC (Figs. 14 and 15). Trajectories are initialized in a 5.5 km \times 2.0 km horizontal plane with 25-m spacing between initial trajectory positions. Backward integration is performed using a fourth-order Runge–Kutta scheme, with linear interpolation in time between successive EnKF analyses and trilinear interpolation in space. A computational time step of 1 s is utilized and trajectories are initialized away from strong convergence near the low-level vertical vorticity maximum and RFD gust front in an attempt to minimize error and prevent the development of spurious “inflow” trajectories (Dahl et al. 2012). Despite these precautions, some inflow trajectories, originating to the south and east of the RFD surge, are still apparent in the resulting analyses and are removed by applying an arbitrary northern threshold to trajectory location following 4 min of backward integration. (Trajectories that fall below the lowest grid level are integrated backward according to the wind values at that level, but are removed from time series analyses presented in Fig. 16.)

Backward trajectories from an initial plane 400 m AGL are found to originate below 1 km aloft and to the

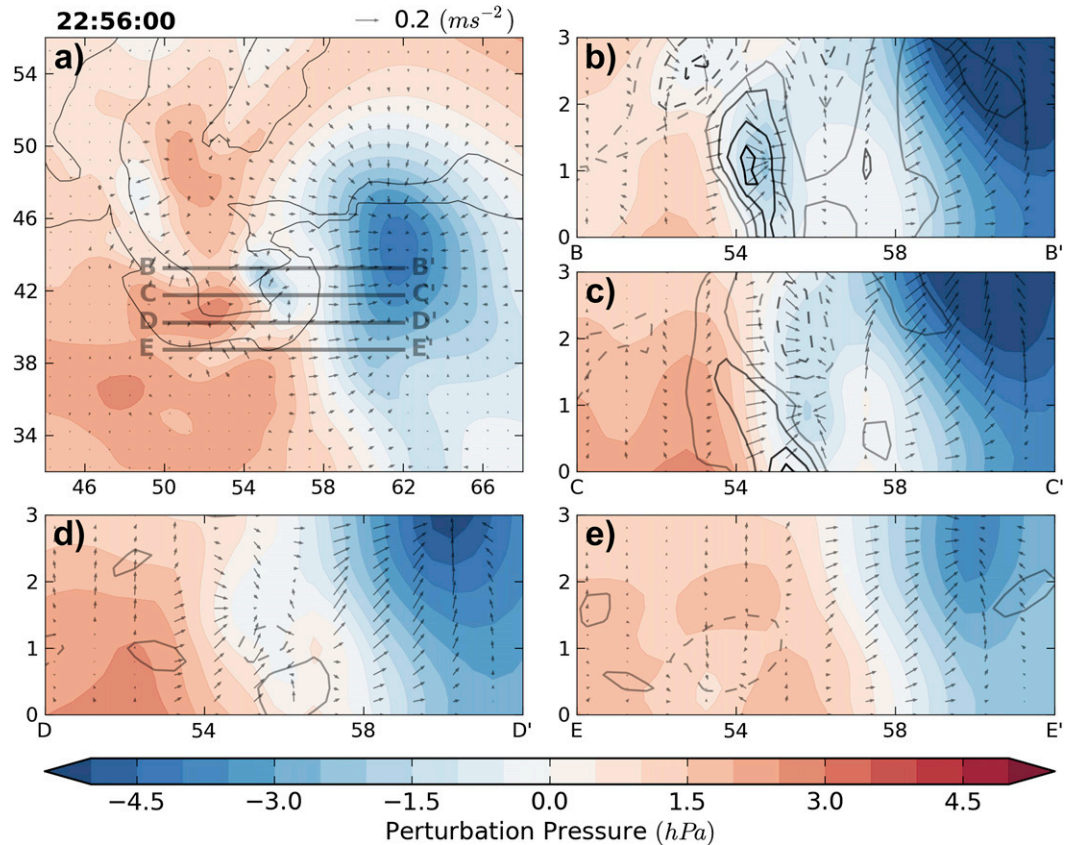


FIG. 12. (a) Perturbation pressure (hPa) 600 m AGL at 2256 UTC is shaded, with simulated reflectivity contoured in black at 20, 40, and 60 dBZ, and vectors indicating horizontal perturbation pressure gradient acceleration (m s^{-2}). (b)–(e) Thick gray lines “B”–“E” represent the position of 0–3-km x – z vertical cross sections. Vertical vorticity is contoured every 0.0075 s^{-1} in (b)–(e), with dashed contours indicating anticyclonic vorticity. Vectors in the cross-sectional plots indicate the x – z perturbation pressure gradient acceleration (m s^{-2}) and are plotted on the same scale as the horizontal cross section. All pressure gradient acceleration vectors have been thinned by a factor of 2 for clarity.

northwest of the low-level mesocyclone, then wrap cyclonically around the mesocyclone with time (Fig. 14). Parcels initially in the southwestern portion of the plane over the southern regions of the internal RFD surge experience an upward excursion to maximum heights slightly above 1 km before rapidly descending between 2256 and 2300 UTC in the region of downdraft trailing the RFD surge gust front. In contrast, parcels initialized over the northern portion of the RFD surge remain below 500 m aloft through the backward integration and originate in the northwestern portions of the low-level mesocyclone. Trajectories initialized ahead of the internal RFD surge gust front remain below 500 m through the backward integration and experience less horizontal displacement than other regions, originating near the southwestern extent of the low-level mesocyclone. This slower evolution is consistent with deceleration of air parcels as they cross the trough axis trailing the RFD surge gust front.

A second source region becomes apparent if the initial trajectory plane is placed farther aloft at 600 m AGL (Fig. 15). Parcels initialized in the southwestern portions of the RFD surge originate from altitudes up to 2 km aloft, and farther to the southwest than the remainder of the trajectories, before descending in the region of high pressure and downward perturbation pressure gradient acceleration trailing the pressure trough (Figs. 9c–e and 13e). The generally increasing origin height of trajectories moving from east to west within the RFD (Figs. 14 and 15) is similar to dual-Doppler trajectories within the RFD calculated by Markowski et al. (2012a) and Kosiba et al. (2013).

Time series of the trajectory heights and u , v , and w components of the wind speed reveal a similar evolution to trajectories released at 400 and 600 m, with an obvious exception for parcels originating in the second source region aloft (Fig. 16). All trajectories experience a net acceleration in zonal wind speed over the course of the

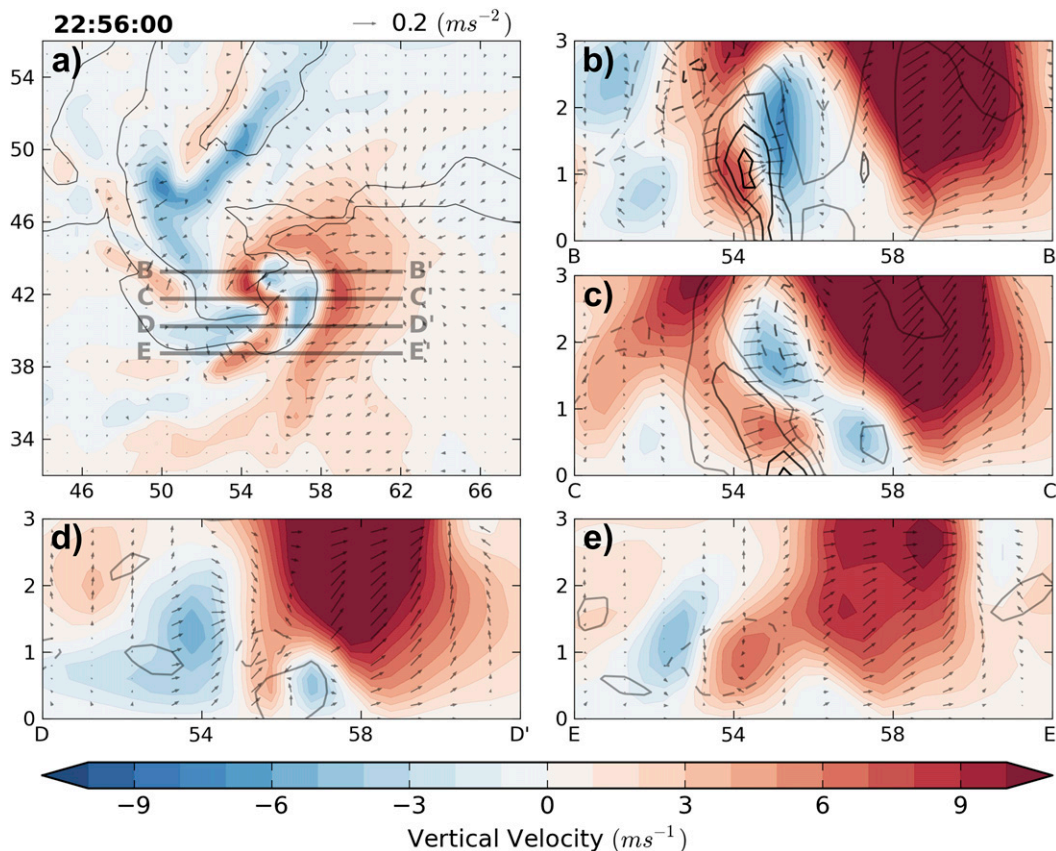


FIG. 13. As in Fig. 12, but vertical velocity is contoured in place of perturbation pressure.

integration period consistent with a favorable horizontal perturbation pressure gradient force. Despite a net acceleration through the period, some trajectories experience a deceleration in zonal wind speed between 2256 and 2300 UTC, representative of encountering an adverse horizontal perturbation pressure gradient force as they cross the trough axis. Most parcels experience smaller meridional accelerations, with two exceptions. A group of near-surface parcels experience a northward acceleration through the second half of the integration period, resulting in a southerly component to the wind speed by 2300 UTC consistent with parcels wrapping cyclonically around the low-level mesocyclone. Second, the parcels from the secondary source region experience a dramatic meridional acceleration from southerly at nearly 20 m s^{-1} at 2250 UTC to northerly at 10 m s^{-1} at 2300 UTC (Fig. 16). The initial southwesterly wind direction at approximately 2 km AGL of parcels in the secondary source region matches the environmental wind profile (Fig. 3), suggesting that they originate in the ambient environment. Additionally, parcels from this region descend while embedded in a region of high pressure and downward-directed perturbation pressure gradient acceleration trailing the RFD surge gust front

between 1 and 2 km aloft (e.g., Figs. 12e and 13e), which resembles the evolution of recent simulated RFD surges by Schenkman et al. (2014a).

5. Summary and discussion

The development of an internal RFD momentum surge and associated gust front in the 18 May 2010, Dumas, Texas, supercell has been found to be primarily driven by the nonlinear dynamic component of the perturbation pressure at low levels. The occluded low-level mesocyclone and mesoanticyclone trail the primary RFD surge gust front by several kilometers throughout the 10-min period of interest (Figs. 5 and 6), with the strong south–north tilt of both circulations resulting in a local maximum in the magnitude of vertical vorticity bridging the two maxima (Figs. 12 and 13). This region of locally enhanced vorticity magnitude is associated with a trough of low nonlinear dynamic perturbation pressure (Figs. 9 and 11), which is represented schematically in Fig. 17a. This perturbation pressure field causes parcels originating near the surface northwest of the low-level mesocyclone (Fig. 14) to experience a favorable horizontal perturbation pressure

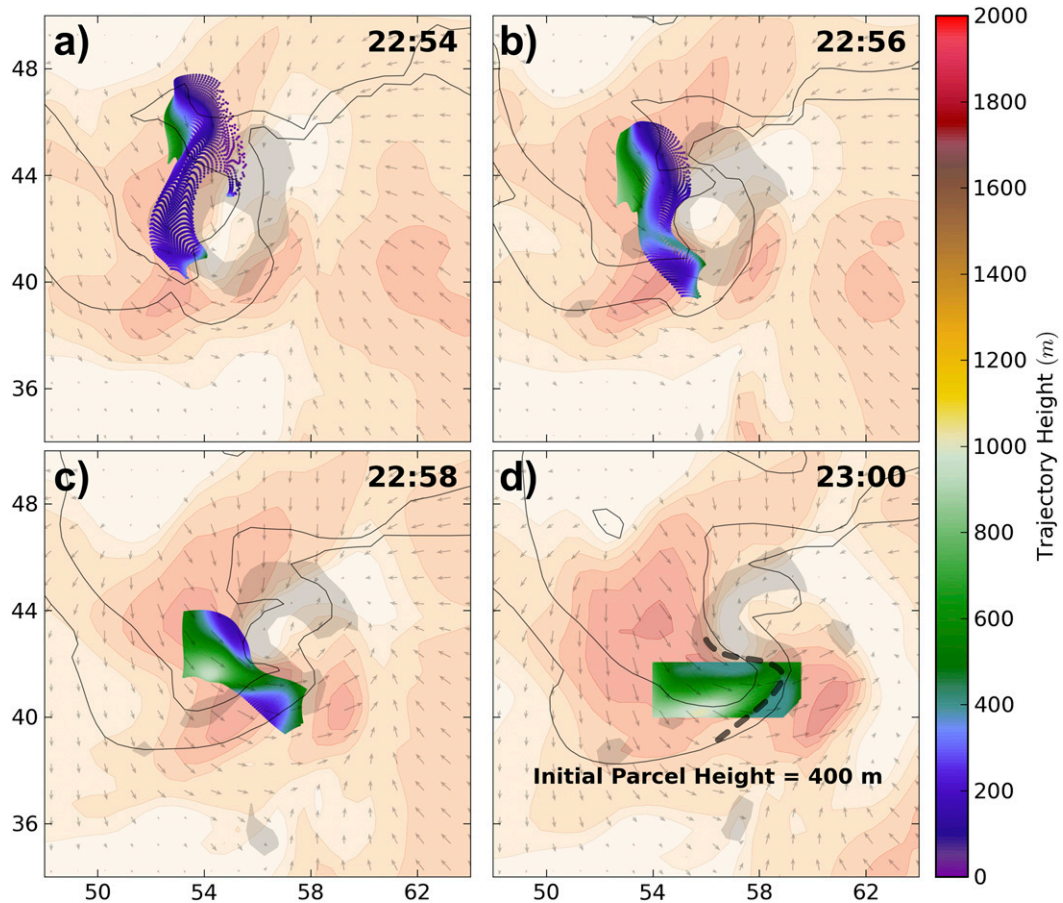


FIG. 14. Scatterplot of x - y backward trajectory position for a trajectory plane initialized at 2300 UTC and 400 m AGL at (a) 2254, (b) 2256, (c) 2258, and (d) 2300 UTC. Overlap in trajectory scatterplots creates the impression of shading in regions of high trajectory density. Trajectories in (a)–(c) are color coded according to their height AGL at the given time, and trajectories in (d) are color coded according to their maximum height during the 2250–2300 UTC integration. Trajectory positions are overlain on near-surface wind speed plots as in Figs. 5 and 6, although with increased transparency for improved clarity. Simulated reflectivity values of 20, 40, and 60 dBZ are contoured in black and cyclonic vertical vorticity greater than 0.0075 s^{-1} is shaded gray. The subjectively analyzed position of the internal RFD surge gust front is plotted with a thick, dashed line in (d).

gradient acceleration as they wrap cyclonically around the low-level mesocyclone (Fig. 16). These parcels then experience an adverse horizontal perturbation pressure gradient acceleration upon crossing the trough axis. This adverse pressure gradient acceleration results in a rapid deceleration of the horizontal wind leading the trough axis and the development of a local maximum in horizontal momentum within the broadscale RFD bounded by a convergence zone on its leading edge, representing an internal RFD momentum surge (Fig. 17b).

Backward trajectories initialized in the region of maximum low-level, horizontal wind speeds within the RFD are found to remain below 1 km AGL in the preceding 10 min and accelerate by means of a horizontal perturbation pressure gradient force (Figs. 9, 12, 13, 14, and 16); which resembles the development of simulated

severe straight-line winds near bow-echo mesovortices (Trapp and Weisman 2003). As the RFD to the south of the low-level mesocyclone is a favored region for straight-line winds in supercells (e.g., Fujita 1989; Karstens et al. 2013), it appears possible that some damaging straight-line winds in supercells develop similarly to those associated with a bow-echo mesovortex (Trapp and Weisman 2003) rather than the downburst mechanism more commonly applied to straight-line wind damage (e.g., Fujita 1985).

An additional source region for air parcels within the southern and western extent of the RFD surge is found approximately 2 km aloft. Similarly to simulations by Schenkman et al. (2014a), these parcels originate in the environmental southwesterlies before descending rapidly in a region of high perturbation pressure within the

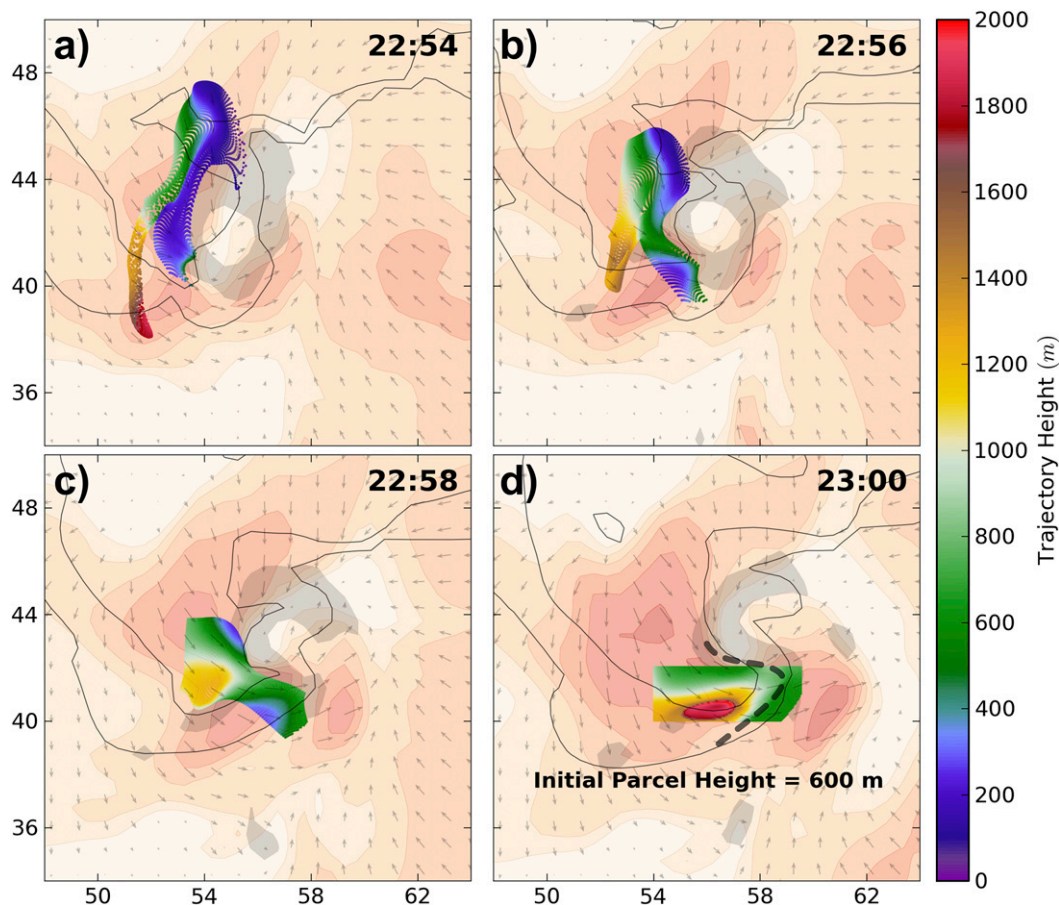


FIG. 15. As in Fig. 14, but for a trajectory plane initialized at 600 m AGL.

RFD surge (Figs. 12, 13, 15, and 16). A difference between the Schenkman et al. (2014a) simulations and those presented here is that Schenkman et al. (2014a) found trajectories originating from the near-storm environment aloft descended to near the surface within the RFD momentum surge, whereas the ones here do not descend below 500 m AGL (Fig. 16). However, observed differences in kinematic and thermodynamic properties of successive RFD surges (e.g., Lee et al. 2012) suggests source regions of air parcels within an RFD surge may vary over the life cycle of a supercell and both regions identified herein are a viable source region for near-surface air parcels in RFD surges.

The downdraft associated with the source region trailing the internal RFD gust front occurs coincident with downward dynamic perturbation pressure gradient acceleration over the southwestern portions of the mesocyclone (Fig. 10). This downdraft was hypothesized to be an occlusion downdraft in S14; however, a downdraft within a region of nonlinear dynamic downward acceleration to the southeast of the low-level mesocyclone and leading the internal RFD surge gust front is present

throughout the period of interest, consistent with occlusion downdrafts in prior simulations (Klemp and Rotunno 1983; Wicker and Wilhelmson 1995; Adlerman et al. 1999). Despite the presence of this more prototypical occlusion downdraft separate from the RFD surge, downward motion within the surge is partially driven by similar dynamic forcing. Therefore, the RFD surge in the Dumas supercell can be considered either the surface manifestation of a second occlusion downdraft or a separate downdraft within downward dynamic perturbation pressure gradient acceleration.

The grid spacing in the EnKF experiments was not sufficient to resolve the multiple internal RFD momentum surges documented by S14 (Fig. 7). However, RFD surges driven by horizontal nonlinear dynamic perturbation pressure gradient accelerations can be expected to vary in intensity according to the magnitude of rotationally induced pressure gradient near the low-level mesocyclone. We speculate that several storm-scale processes could induce periodic variation to the horizontal perturbation pressure gradient field and successive, reinforcing internal RFD momentum surges

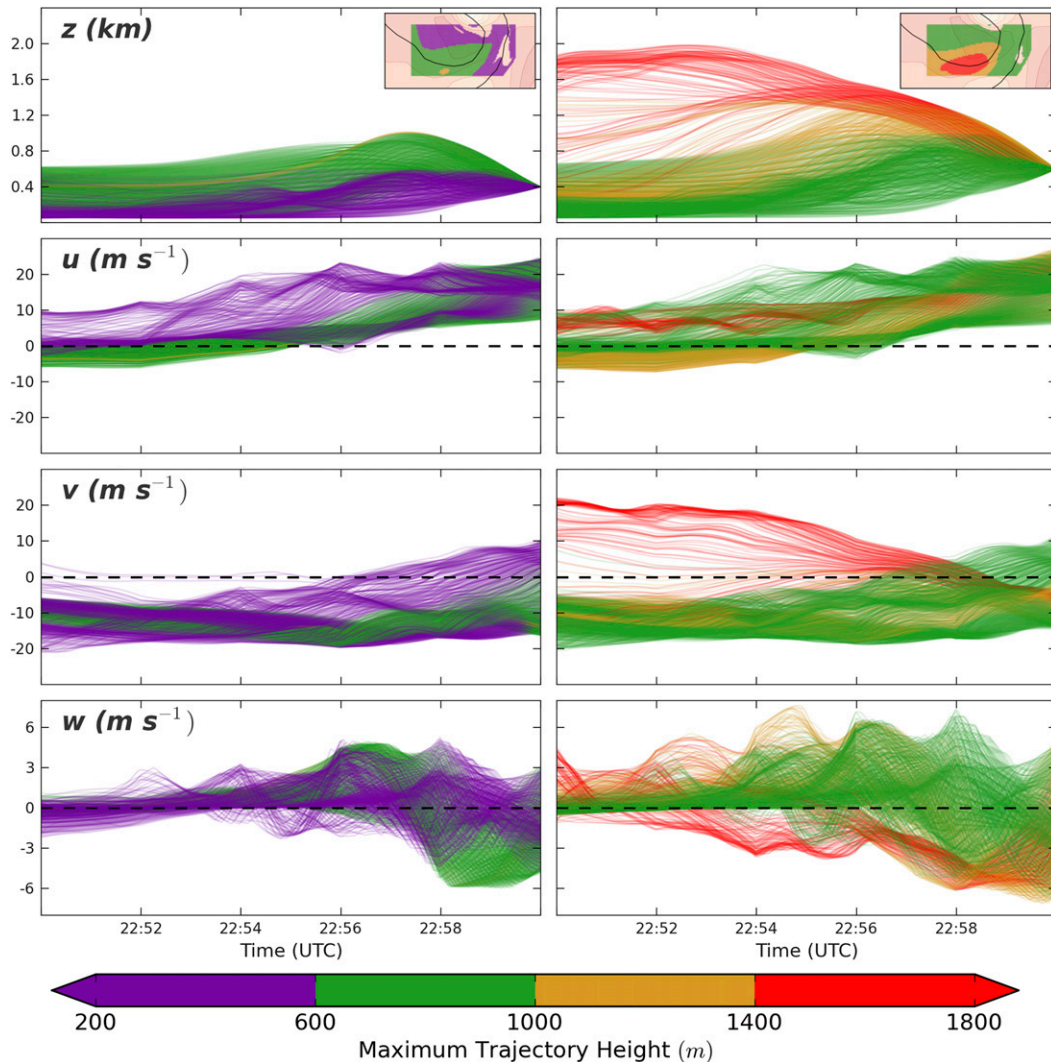


FIG. 16. Time series plots of (from top to bottom) trajectory height (km), zonal wind speed (m s^{-1}), meridional wind speed (m s^{-1}), and vertical wind speed (m s^{-1}) for trajectory planes initialized at (left) 400 and (right) 600 m AGL. Trajectories are color coded according to their maximum height during the 10-min integration, trajectories that fall below the lowest model level are excluded from the plots, and every fifth trajectory is plotted for clarity. Insets in the top row provide initial trajectory locations at 2300 UTC, color coded according to maximum height, and overlaid on wind speed and simulated reflectivity contours as in Figs. 14 and 15.

such as those in the Dumas supercell; including a multiple-vortex mesocyclone (Wakimoto and Liu 1998; Wurman and Kosiba 2013; Figs. 5 and 6), secondary vorticity maxima propagating down the occluded portion of the primary RFD gust front (Richardson et al. 2012), or rotation of a tornado or tornado cyclone within a broader low-level mesocyclone (Wakimoto et al. 2003; Marquis et al. 2008; Wurman and Kosiba 2013).

The occluded low-level mesocyclone, companion mesoanticyclone, and associated pressure trough are displaced rearward from the primary RFD gust front in the initial analyses of the Dumas supercell, preventing a diagnosis of the initial trough development. However,

the initial occlusion of the low-level mesocyclone and primary RFD gust front would be expected to force the minima of rotationally induced low pressure rearward with respect to the primary RFD gust front, and may result in the development of a trough within the broadscale RFD. There appears to be subtle evidence of this process in pressure retrievals of an occluding low-level mesocyclone in the 5 June 2009, Goshen County, Wyoming, supercell (Markowski et al. 2012b, see their Fig. 2), which immediately preceded the development of an internal RFD momentum surge (Kosiba et al. 2013).

The analyses presented in this study comprise a 10-min period during a single supercell. More analyses of

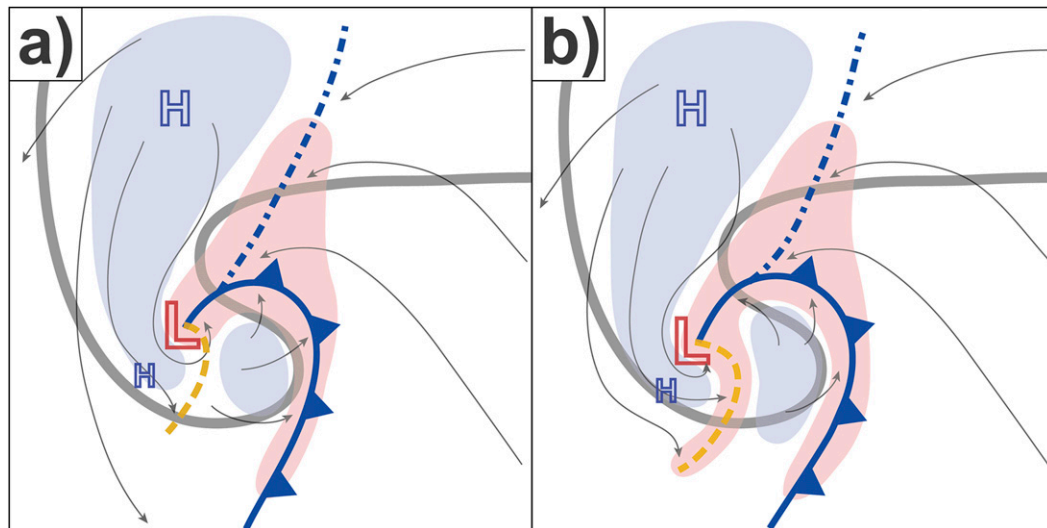


FIG. 17. Idealized schematic of low-level internal RFD momentum surge and associated gust front development in the Dumas supercell. Red (blue) shading indicates regions of updraft (downdraft), with “H” (“L”) annotations identifying regions of locally high (low) perturbation pressure and the primary RFD gust front, forward-flank gust front, and internal RFD surge gust front annotated as a cold front, blue, stippled line, and pressure trough, respectively. Storm precipitation is outlined with a thick, gray contour and idealized streamlines are included as thin, gray arrows. (a) Initial rearward displacement of the low pressure trough from the primary RFDGF for an occluded low-level mesocyclone followed by (b) the development of an internal RFD gust front along the trough axis.

the forcing mechanisms and source regions for RFD surges in multiple supercells, as well as successive surges in a single supercell are needed to assess the representativeness of the results presented here. Additionally, longitudinal studies using either a combination of in situ and dual-Doppler observations or data assimilation retrievals will help define modes of RFD surge evolution and their sensitivity, if any, to storm mode and environmental conditions. Finally, high-resolution representations of successive RFD surges associated with a single low-level mesocyclone, either in observations or numerical simulations, are needed to assess the development of periodic, reinforcing internal RFD momentum surges. Improved understanding of RFD surge formation, environmental sensitivity, and periodicity is expected to lead to improved understanding of associated modes of tornado genesis, maintenance, and decay.

Acknowledgments. We thank Drs. Josh Wurman, Karen Kosiba, and Michael Biggerstaff for collecting and making available the DOW and SMART-R data used in this study and NCAR/EOL, under sponsorship of the National Science Foundation, for hosting the data. Collaboration on the observational aspects of the Dumas case with Drs. Michael French, Howard Bluestein, Paul Markowski, and Yvette Richardson provided much of the motivation and direction for this research. Additionally, we are grateful for thorough reviews of the manuscript provided by Dr. James Marquis and two

anonymous reviewers, as well as conversations with Bruce Lee, Cathy Finley, Anthony Reinhart, Alex Schenkman, Brian Ancell, John Schroeder, and Dan Dawson, which have been invaluable to the research. SOLO II and the Observational Processing and Wind Synthesis (OPAWS) software were used for editing and objectively analyzing radar data and MatLab was used for three-dimensional data visualization. The authors thank the developers of the freely provided Enthought python distribution and matplotlib, NumPy, and SciPy libraries, which were used to produce the majority of the analyses and figures herein. This study was supported by NSF Grants AGS-0800542 and AGS-0964088 to Texas Tech University and the first author received support from a National Research Council Research Associateship.

APPENDIX

Pressure Analysis

The anelastic diagnostic pressure equation solved to retrieve the perturbation pressure is derived by linearizing the components of the wind field around the initial profile, then taking the divergence of the resulting inviscid vertical momentum equation (e.g., Rotunno and Klemp 1982; Klemp and Rotunno 1983). The Poisson equation for diagnostic pressure is then decomposed into three separate Poisson equations

representing the linear dynamic, nonlinear dynamic, and buoyant components of the perturbation pressure [Eq. (1)] given by

$$\nabla^2 \pi'_l = -2 \left(\frac{\partial w'}{\partial x} \frac{\partial \bar{u}}{\partial z} + \frac{\partial w'}{\partial y} \frac{\partial \bar{v}}{\partial z} \right), \tag{A1}$$

$$\nabla^2 \pi'_{nl} = - \left(\frac{\partial u'}{\partial x} \right)^2 - \left(\frac{\partial v'}{\partial y} \right)^2 - \left(\frac{\partial w'}{\partial z} \right)^2 - 2 \left(\frac{\partial v'}{\partial x} \frac{\partial u'}{\partial y} + \frac{\partial w'}{\partial x} \frac{\partial u'}{\partial z} + \frac{\partial w'}{\partial y} \frac{\partial v'}{\partial z} \right), \text{ and} \tag{A2}$$

$$\nabla^2 \pi'_B = \frac{\partial B}{\partial z}, \tag{A3}$$

where the overbar and tick marks indicate base state and perturbation values, respectively.

Each equation is solved in the same manner as in Rotunno and Klemp (1982), Klemp and Rotunno (1983), and Rotunno and Klemp (1985), with the right-hand side evaluated using finite differences of EnKF analyses interpolated to a grid with uniform, 200-m vertical spacing. Software from the FISHPACK FORTRAN libraries developed by the National Center for Atmospheric Research (Swarztrauber et al. 1999) is used to solve for the perturbation pressures by Fourier transforming the right-hand side in the horizontal directions, second-order differencing in the vertical, inverting the resulting tridiagonal matrix, and inverse Fourier transforming the results.

Dirichlet horizontal boundary conditions are applied and vertical boundary conditions identical to Klemp and Rotunno (1983) are used:

$$\left. \frac{\partial \pi_{\text{dyn}}}{\partial z} \right|_{z=0} = 0, \quad \left. \frac{\partial \pi_{\text{dyn}}}{\partial z} \right|_{z=z_T} = 0, \quad \text{and} \tag{A4}$$

$$\left. \frac{\partial \pi_B}{\partial z} \right|_{z=0} = B(x, y, 0), \quad \left. \frac{\partial \pi_B}{\partial z} \right|_{z=z_T} = B(x, y, z_T), \tag{A5}$$

where π_{dyn} represents both the linear and nonlinear dynamic components and z_T is the height of the upper boundary. Perturbation pressures are solved for each ensemble member, then the domain-wide mean perturbation pressure is removed from each member to ensure a unique solution and the resulting pressure fields are averaged to produce the ensemble mean. Retrieved pressures were found to be relatively insensitive to small variations in the horizontal and vertical domain, with maximum changes in retrieved dynamic pressure (dynamic vertical perturbation pressure gradient acceleration) remaining below 0.1 hPa ($0.01 \text{ m}^2 \text{ s}^{-2}$) across the Dumas supercell.

REFERENCES

Adlerman, E. J., 2003: Numerical simulations of cyclic storm behavior: Mesocyclogenesis and tornadogenesis. Ph.D. thesis, University of Oklahoma, 217 pp. [Available from School of Meteorology, University of Oklahoma, 120 David L. Boren Blvd., Suite 5900, Norman, OK 73072.]

—, K. K. Droegemeier, and R. Davies-Jones, 1999: A numerical simulation of cyclic mesocyclogenesis. *J. Atmos. Sci.*, **56**, 2045–2069, doi:10.1175/1520-0469(1999)056<2045:ANSOCM>2.0.CO;2.

Aksoy, A. D., D. Dowell, and C. Snyder, 2009: A multicase comparative assessment of the ensemble Kalman filter for assimilation of radar observations. Part I: Storm-scale analyses. *Mon. Wea. Rev.*, **137**, 1805–1824, doi:10.1175/2008MWR2691.1.

Biggerstaff, M. I., and Coauthors, 2005: The Shared Mobile Atmospheric Research and Teaching Radar: A collaboration to enhance research and teaching. *Bull. Amer. Meteor. Soc.*, **86**, 1263–1274, doi:10.1175/BAMS-86-9-1263.

Bluestein, H. B., M. M. French, I. PopStefanija, R. T. Bluth, and J. B. Knorr, 2010: A mobile, phased-array Doppler radar for the study of severe convective storms. *Bull. Amer. Meteor. Soc.*, **91**, 579–600, doi:10.1175/2009BAMS2914.1.

—, J. B. Houser, M. M. French, J. C. Snyder, G. D. Emmitt, I. PopStefanija, C. Baldi, and R. T. Bluth, 2014: Observations of the boundary layer near tornadoes and in supercells using a mobile, collocated, pulsed Doppler lidar and radar. *J. Atmos. Oceanic Technol.*, **31**, 302–325, doi:10.1175/JTECH-D-13-00112.1.

Caya, A., J. Sun, and C. Snyder, 2005: A comparison between the 4DVAR and ensemble Kalman filter techniques for radar data assimilation. *Mon. Wea. Rev.*, **133**, 3081–3094, doi:10.1175/MWR3021.1.

Coniglio, M. C., D. J. Stensrud, and L. J. Wicker, 2006: Effects of upper-level shear on the structure and maintenance of strong quasi-linear mesoscale convective systems. *J. Atmos. Sci.*, **63**, 1231–1252, doi:10.1175/JAS3681.1.

Dahl, J. M. L., M. D. Parker, and L. J. Wicker, 2012: Uncertainties in trajectory calculations within near-surface mesocyclones of simulated supercells. *Mon. Wea. Rev.*, **140**, 2959–2966, doi:10.1175/MWR-D-12-00131.1.

—, —, and —, 2014: Imported and storm-generated near-ground vertical vorticity in a simulated supercell. *J. Atmos. Sci.*, **71**, 3027–3051, doi:10.1175/JAS-D-13-0123.1.

Dawson, D. T., II, L. J. Wicker, E. R. Mansell, and R. L. Tanamachi, 2012: Impact of the environmental low-level wind profile on ensemble forecasts of the 4 May 2007 Greensburg, Kansas, tornadic storm and associated mesocyclones. *Mon. Wea. Rev.*, **140**, 696–716, doi:10.1175/MWR-D-11-00008.1.

Dowell, D. C., and L. J. Wicker, 2009: Additive noise for storm-scale ensemble data assimilation. *J. Atmos. Oceanic Technol.*, **26**, 911–927, doi:10.1175/2008JTECHA1156.1.

—, F. Zhang, L. J. Wicker, C. Snyder, and N. A. Crook, 2004: Wind and temperature retrievals in the 17 May 1981 Arcadia, Oklahoma, supercell: Ensemble Kalman filter experiments. *Mon. Wea. Rev.*, **132**, 1982–2005, doi:10.1175/1520-0493(2004)132<1982:WATRIT>2.0.CO;2.

—, L. J. Wicker, and C. Snyder, 2011: Ensemble Kalman filter assimilation of radar observations of the 8 May 2003 Oklahoma City supercell: Influences of reflectivity observations on storm-scale analyses. *Mon. Wea. Rev.*, **139**, 272–294, doi:10.1175/2010MWR3438.1.

- Evensen, G., 1994: Sequential data assimilation with a nonlinear quasi-geostrophic model using Monte Carlo methods to forecast error statistics. *J. Geophys. Res.*, **99**, 10 143–10 162, doi:10.1029/94JC00572.
- Finley, C. A., and B. D. Lee, 2004: High resolution mobile mesonet observations of RFD surges in the June 9 Basset, Nebraska supercell during Project ANSWERS 2003. *22nd Conf. on Severe Local Storms*, Hyannis, MA, Amer. Meteor. Soc., P11.3. [Available online at https://ams.confex.com/ams/11aram22sls/techprogram/paper_82005.htm.]
- French, M. M., H. B. Bluestein, I. PopStefanija, C. Baldi, and R. T. Bluth, 2013: Reexamining the vertical development of Tornadic Vortex Signatures in supercells. *Mon. Wea. Rev.*, **141**, 4576–4601, doi:10.1175/MWR-D-12-00315.1.
- Fujita, T. T., 1985: The downburst: Microburst and macroburst. SMRP Research Paper 210, University of Chicago, 51 pp.
- , 1989: The Teton–Yellowstone tornado of 21 July 1987. *Mon. Wea. Rev.*, **117**, 1913–1940, doi:10.1175/1520-0493(1989)117<1913:TTYTOJ>2.0.CO;2.
- Gaspari, G., and S. E. Cohn, 1999: Construction of correlation functions in two and three dimensions. *Quart. J. Roy. Meteor. Soc.*, **125**, 723–757, doi:10.1002/qj.49712555417.
- Hirth, B. D., J. L. Schroeder, and C. C. Weiss, 2008: Surface analysis of the rear-flank downdraft outflow in two tornadic supercells. *Mon. Wea. Rev.*, **136**, 2344–2363, doi:10.1175/2007MWR2285.1.
- , —, W. S. Gunter, and J. G. Guynes, 2012: Measuring a utility scale turbine wake using the TTUKa mobile research radars. *J. Atmos. Oceanic Technol.*, **29**, 765–771, doi:10.1175/JTECH-D-12-00039.1.
- Houser, J. L., H. B. Bluestein, and J. C. Snyder, 2015: Rapid-scan, polarimetric, Doppler radar observations of tornadogenesis and tornado dissipation in a tornadic supercell: The “El Reno, Oklahoma” storm of 24 May 2011. *Mon. Wea. Rev.*, **143**, 2685–2710, doi:10.1175/MWR-D-14-00253.1.
- Houtekamer, P. L., and H. L. Mitchell, 1998: Data assimilation using and ensemble Kalman filter technique. *Mon. Wea. Rev.*, **126**, 796–811, doi:10.1175/1520-0493(1998)126<0796:DAUAEK>2.0.CO;2.
- Karstens, C. D., T. M. Samaras, B. D. Lee, W. A. Gallus, and C. A. Finley, 2010: Near-ground pressure and wind measurements in tornadoes. *Mon. Wea. Rev.*, **138**, 2570–2588, doi:10.1175/2010MWR3201.1.
- , W. A. Gallus Jr., B. D. Lee, and C. A. Finley, 2013: Analysis of tornado-induced tree fall using aerial photography from the Joplin, Missouri, and Tuscaloosa–Birmingham, Alabama, tornadoes of 2011. *J. Appl. Meteor. Climatol.*, **52**, 1049–1068, doi:10.1175/JAMC-D-12-0206.1.
- Klemp, J. B., and R. Rotunno, 1983: A study of the tornadic region within a supercell thunderstorm. *J. Atmos. Sci.*, **40**, 359–377, doi:10.1175/1520-0469(1983)040<0359:ASOTTR>2.0.CO;2.
- Kosiba, K. A., J. Wurman, Y. Richardson, P. Markowski, P. Robinson, and J. Marquis, 2013: Genesis of the Goshen County, Wyoming, tornado on 5 June 2009 during VORTEX2. *Mon. Wea. Rev.*, **141**, 1157–1181, doi:10.1175/MWR-D-12-00056.1.
- Kurdzo, J. M., D. J. Bodine, B. L. Cheong, and R. D. Palmer, 2015: High-temporal resolution polarimetric X-band Doppler radar observations of the 20 May 2013 Moore, Oklahoma, tornado. *Mon. Wea. Rev.*, **143**, 2711–2735, doi:10.1175/MWR-D-14-00357.1.
- Lee, B. D., C. A. Finley, and P. Skinner, 2004: Thermodynamic and kinematic analysis of multiple RFD surges for the 24 June 2003 Manchester, SD cyclic tornadic supercell during Project ANSWERS 2003. *22nd Conf. on Severe Local Storms*, Hyannis, MA, Amer. Meteor. Soc., P11.2. [Available online at https://ams.confex.com/ams/11aram22sls/techprogram/paper_82000.htm.]
- , —, and T. M. Samaras, 2011: Surface analysis near and within the Tipton, Kansas, tornado on 29 May 2008. *Mon. Wea. Rev.*, **139**, 370–386, doi:10.1175/2010MWR3454.1.
- , —, and C. D. Karstens, 2012: The Bowdle, South Dakota, cyclic tornadic supercell of 22 May 2010: Surface analysis of rear-flank downdraft evolution and multiple internal surges. *Mon. Wea. Rev.*, **140**, 3419–3441, doi:10.1175/MWR-D-11-00351.1.
- Mahale, V. N., J. A. Brotzge, and H. B. Bluestein, 2014: The advantages of a mixed-band radar network for severe weather operations: A case study of 13 May 2009. *Wea. Forecasting*, **29**, 78–98, doi:10.1175/WAF-D-13-00024.1.
- Majcen, M., P. Markowski, Y. Richardson, D. Dowell, and J. Wurman, 2008: Multipass objective analysis of Doppler radar data. *J. Atmos. Oceanic Technol.*, **25**, 1845–1858, doi:10.1175/2008JTECHA1089.1.
- Mansell, E. R., C. L. Ziegler, and E. C. Bruning, 2010: Simulated electrification of a small thunderstorm with two-moment bulk microphysics. *J. Atmos. Sci.*, **67**, 171–194, doi:10.1175/2009JAS2965.1.
- Markowski, P. M., and Y. P. Richardson, 2014: The influence of environmental low-level shear and cold pools on tornadogenesis: Insights from toy simulations. *J. Atmos. Sci.*, **71**, 243–275, doi:10.1175/JAS-D-13-0159.1.
- , and Coauthors, 2012a: The pretornadic phase of the Goshen County, Wyoming, supercell of 5 June 2009 intercepted by VORTEX2. Part I: Evolution of kinematic and surface thermodynamic fields. *Mon. Wea. Rev.*, **140**, 2887–2915, doi:10.1175/MWR-D-11-00336.1.
- , and Coauthors, 2012b: The pretornadic phase of the Goshen County, Wyoming, supercell of 5 June 2009 intercepted by VORTEX2. Part II: Intensification of low-level rotation. *Mon. Wea. Rev.*, **140**, 2916–2938, doi:10.1175/MWR-D-11-00337.1.
- , J. M. Straka, E. N. Rasmussen, R. P. Davies-Jones, Y. Richardson, and J. Trapp, 2008: Vortex lines within low-level mesocyclones obtained from pseudo-dual-Doppler radar observations. *Mon. Wea. Rev.*, **136**, 3513–3535, doi:10.1175/2008MWR2315.1.
- Marquis, J., Y. Richardson, J. Wurman, and P. M. Markowski, 2008: Single- and dual-Doppler analysis of a tornadic vortex and surrounding storm-scale flow in the Crowell, Texas, supercell of 30 April 2000. *Mon. Wea. Rev.*, **136**, 5017–5043, doi:10.1175/2008MWR2442.1.
- , Y. P. Richardson, P. M. Markowski, D. C. Dowell, and J. Wurman, 2012: Tornado maintenance investigated with high-resolution dual-Doppler and EnKF analysis. *Mon. Wea. Rev.*, **140**, 3–27, doi:10.1175/MWR-D-11-00025.1.
- , —, —, —, —, K. Kosiba, P. Robinson, and G. Romine, 2014: An investigation of the Goshen County, Wyoming, tornadic supercell of 5 June 2009 using EnKF assimilation of mobile mesonet and radar observations collected during VORTEX2. Part I: Experiment design and verification of the EnKF analyses. *Mon. Wea. Rev.*, **142**, 530–554, doi:10.1175/MWR-D-13-00007.1.
- Mashiko, W., H. Niino, and T. Kato, 2009: Numerical simulation of tornadogenesis in an outer-rainband minisupercell of Typhoon Shanshan on 17 September 2006. *Mon. Wea. Rev.*, **137**, 4238–4260, doi:10.1175/2009MWR2959.1.

- Parker, M. D., 2014: Composite VORTEX2 supercell environments from near-storm soundings. *Mon. Wea. Rev.*, **142**, 508–529, doi:10.1175/MWR-D-13-00167.1.
- Potvin, C. K., and L. J. Wicker, 2012: Comparison between dual-Doppler and EnKF storm-scale wind analyses: Observing system simulation experiments with a supercell thunderstorm. *Mon. Wea. Rev.*, **140**, 3972–3991, doi:10.1175/MWR-D-12-00044.1.
- , and —, 2013a: Assessing ensemble forecasts of low-level supercell rotation within an OSSE framework. *Wea. Forecasting*, **28**, 940–960, doi:10.1175/WAF-D-12-00122.1.
- , and —, 2013b: Correcting fast-mode pressure errors in storm-scale ensemble Kalman filter analyses. *Adv. Meteor.*, **2013**, 624931, doi:10.1155/2013/624931.
- , —, D. Betten, M. I. Biggerstaff, and A. Shapiro, 2013: Comparison between dual-Doppler and EnKF storm-scale wind analyses: The 29–30 May 2004 Geary, Oklahoma, supercell thunderstorm. *Mon. Wea. Rev.*, **141**, 1612–1628, doi:10.1175/MWR-D-12-00308.1.
- Richardson, Y. P., P. Markowski, J. N. Marquis, J. Wurman, K. A. Kosiba, P. Robinson, D. W. Burgess, and C. C. Weiss, 2012: Tornado maintenance and demise in the Goshen County, Wyoming supercell of 5 June 2009 intercepted by VORTEX2. *26th Conf. on Severe Local Storms*, Nashville, TN, Amer. Meteor. Soc., 12.2. [Available online at <https://ams.confex.com/ams/15MESO/webprogram/Paper228075.html>.]
- Rotunno, R., 1984: An investigation of a three-dimensional axisymmetric vortex. *J. Atmos. Sci.*, **41**, 283–298, doi:10.1175/1520-0469(1984)041<0283:AIOATD>2.0.CO;2.
- , and J. B. Klemp, 1982: The influence of shear-induced pressure gradient on thunderstorm motion. *Mon. Wea. Rev.*, **110**, 136–151, doi:10.1175/1520-0493(1982)110<0136:TIOTSI>2.0.CO;2.
- , and —, 1985: On the rotation and propagation of simulated supercell thunderstorms. *J. Atmos. Sci.*, **42**, 271–292, doi:10.1175/1520-0469(1985)042<0271:OTRAPO>2.0.CO;2.
- Schenkman, A. D., M. Xue, D. T. Dawson, and M. Hu, 2014a: Internal momentum surges in a high-resolution simulation of the 8 May 2003 Oklahoma City tornadic supercell. *27th Conf. on Severe Local Storms*, Madison, WI, Amer. Meteor. Soc., 12A.3. [Available online at <https://ams.confex.com/ams/27SLS/webprogram/Paper255956.html>.]
- , —, and M. Hu, 2014b: Tornadogenesis in a high-resolution simulation of the 8 May 2003 Oklahoma City supercell. *J. Atmos. Sci.*, **71**, 130–154, doi:10.1175/JAS-D-13-073.1.
- Schroeder, J. L., and C. C. Weiss, 2008: Integrating research and education through measurement and analysis. *Bull. Amer. Meteor. Soc.*, **89**, 793–798, doi:10.1175/2008BAMS2287.1.
- Skinner, P. S., C. C. Weiss, J. L. Schroeder, L. J. Wicker, and M. I. Biggerstaff, 2011: Observations of the surface boundary structure within the 23 May 2007 Perryton, Texas, supercell. *Mon. Wea. Rev.*, **139**, 3730–3749, doi:10.1175/MWR-D-10-05078.1.
- , —, M. M. French, H. B. Bluestein, P. M. Markowski, and Y. P. Richardson, 2014: VORTEX2 observations of a low-level mesocyclone with multiple internal rear-flank downdraft momentum surges in the 18 May 2010 Dumas, Texas, supercell. *Mon. Wea. Rev.*, **142**, 2935–2960, doi:10.1175/MWR-D-13-00240.1.
- Snyder, C., and F. Zhang, 2003: Assimilation of simulated Doppler radar observations with an ensemble Kalman filter. *Mon. Wea. Rev.*, **131**, 1663–1677, doi:10.1175//2555.1.
- Stensrud, D. J., and Coauthors, 2013: Progress and challenges with Warn-On-Forecast. *Atmos. Res.*, **123**, 2–16, doi:10.1016/j.atmosres.2012.04.004.
- Straka, J. M., E. N. Rasmussen, and S. E. Fredrickson, 1996: A mobile mesonet for finescale meteorological observations. *J. Atmos. Oceanic Technol.*, **13**, 921–936, doi:10.1175/1520-0426(1996)013<0921:AMMFFM>2.0.CO;2.
- , —, R. P. Davies-Jones, and P. M. Markowski, 2007: An observational and idealized numerical examination of low-level counter-rotating vortices toward the rear flank of supercells. *E. J. Severe Storms Meteor.*, **2** (8), 1–22.
- Swarztrauber, P. N., R. A. Sweet, and J. C. Adams, 1999: FISHPACK: Efficient FORTRAN subprograms for the solution of elliptic partial differential equations. Tech. Rep. 1A-109, National Center for Atmospheric Research, 127 pp.
- Tanamachi, R. L., L. J. Wicker, D. C. Dowell, H. B. Bluestein, D. T. Dawson, and M. Xue, 2013: EnKF assimilation of high-resolution, mobile Doppler radar data of the 4 May 2007 Greensburg, Kansas supercell into a numerical cloud model. *Mon. Wea. Rev.*, **141**, 625–648, doi:10.1175/MWR-D-12-00099.1.
- , P. L. Heinselman, and L. J. Wicker, 2015: Impacts of a storm merger on the 24 May 2011 El Reno, Oklahoma, tornadic supercell. *Wea. Forecasting*, **30**, 501–524, doi:10.1175/WAF-D-14-00164.1.
- Tong, M., and M. Xue, 2005: Ensemble Kalman filter assimilation of Doppler radar data with a compressible nonhydrostatic model: OSS experiments. *Mon. Wea. Rev.*, **133**, 1789–1807, doi:10.1175/MWR2898.1.
- Trapp, R. J., 2000: A clarification of vortex breakdown and tornadogenesis. *Mon. Wea. Rev.*, **128**, 888–895, doi:10.1175/1520-0493(2000)128<0888:ACOVBA>2.0.CO;2.
- , and M. L. Weisman, 2003: Low-level mesovortices within squall lines and bow echoes. Part II: Their genesis and implications. *Mon. Wea. Rev.*, **131**, 2804–2823, doi:10.1175/1520-0493(2003)131<2804:LMWSLA>2.0.CO;2.
- Wakimoto, R. M., and C. Liu, 1998: The Garden City, Kansas, storm during VORTEX 95. Part II: The wall cloud and tornado. *Mon. Wea. Rev.*, **126**, 393–408, doi:10.1175/1520-0493(1998)126<0393:TGCKSD>2.0.CO;2.
- , and H. Cai, 2000: Analysis of a nontornadic storm during VORTEX 95. *Mon. Wea. Rev.*, **128**, 565–592, doi:10.1175/1520-0493(2000)128<0565:AOANSD>2.0.CO;2.
- , C. Liu, and H. Cai, 1998: The Garden City, Kansas, storm during VORTEX 95. Part I: Overview of the storm life cycle and mesocyclogenesis. *Mon. Wea. Rev.*, **126**, 372–392, doi:10.1175/1520-0493(1998)126<0372:TGCKSD>2.0.CO;2.
- , H. V. Murphey, D. C. Dowell, and H. B. Bluestein, 2003: The Kellerville tornado during VORTEX: Damage survey and Doppler radar analysis. *Mon. Wea. Rev.*, **131**, 2197–2221, doi:10.1175/1520-0493(2003)131<2197:TKTDVD>2.0.CO;2.
- Waugh, S., and S. E. Fredrickson, 2010: An improved aspirated temperature system for mobile meteorological observations, especially in severe weather. *25th Conf. on Severe Local Storms*, Denver, CO, Amer. Meteor. Soc., P5.2. [Available online at <https://ams.confex.com/ams/25SLS/webprogram/Paper176205.html>.]
- Weiss, C. C., J. L. Schroeder, J. Guynes, P. Skinner, and J. Beck, 2009: The TTUKa mobile Doppler radar: Coordinated radar and in situ measurements of supercell thunderstorms during Project VORTEX2. *34th Conf. on Radar Meteorology*, Williamsport, VA, Amer. Meteor. Soc., 11B.2. [Available online at https://ams.confex.com/ams/34Radar/techprogram/paper_155425.htm.]
- , T. R. Cermak, R. S. Metzger, A. E. Reinhart, and P. S. Skinner, 2014: Insights into tornado structure afforded by high-frequency mobile radar. *27th Conf. on Severe Local Storms*, Madison, WI, Amer. Meteor. Soc., 9.4. [Available

- online at <https://ams.confex.com/ams/27SLS/webprogram/Paper255350.html>.]
- , D. C. Dowell, J. L. Schroeder, P. S. Skinner, A. E. Reinhart, P. M. Markowski, and Y. P. Richardson, 2015: A comparison of near-surface buoyancy and baroclinity across three VORTEX2 supercell intercepts. *Mon. Wea. Rev.*, **143**, 2736–2753, doi:10.1175/MWR-D-14-00307.1.
- Whitaker, J. S., and T. M. Hamill, 2002: Ensemble data assimilation without perturbed observations. *Mon. Wea. Rev.*, **130**, 1913–1924, doi:10.1175/1520-0493(2002)130<1913:EDAWPO>2.0.CO;2.
- Wicker, L. J., and R. B. Wilhelmson, 1995: Simulation and analysis of tornado development and decay within a three-dimensional supercell thunderstorm. *J. Atmos. Sci.*, **52**, 2675–2703, doi:10.1175/1520-0469(1995)052<2675:SAOTD>2.0.CO;2.
- , and W. C. Skamarock, 2002: Time-splitting methods for elastic models using forward time schemes. *Mon. Wea. Rev.*, **130**, 2088–2097, doi:10.1175/1520-0493(2002)130<2088:TSMFEM>2.0.CO;2.
- Wurman, J., and K. Kosiba, 2013: Fine-scale radar observations of tornado and mesocyclone structures. *Wea. Forecasting*, **28**, 1157–1174, doi:10.1175/WAF-D-12-00127.1.
- , J. M. Straka, E. N. Rasmussen, M. Randall, and A. Zahrai, 1997: Design and deployment of a portable, pencil-beam, pulsed, 3-cm Doppler radar. *J. Atmos. Oceanic Technol.*, **14**, 1502–1512, doi:10.1175/1520-0426(1997)014<1502:DADOAP>2.0.CO;2.
- , Y. P. Richardson, C. Alexander, S. Weygant, and P. F. Zhang, 2007: Dual-Doppler and single-Doppler analysis of a tornadic storm undergoing mergers and repeated tornadogenesis. *Mon. Wea. Rev.*, **135**, 736–758, doi:10.1175/MWR3276.1.
- , K. Kosiba, P. Markowski, Y. Richardson, D. Dowell, and P. Robinson, 2010: Fine-scale single- and dual-Doppler analysis of tornado intensification, maintenance, and dissipation in the Orleans, Nebraska, supercell. *Mon. Wea. Rev.*, **138**, 4439–4455, doi:10.1175/2010MWR3330.1.
- , D. Dowell, Y. Richardson, P. Markowski, E. Rasmussen, D. Burgess, L. Wicker, and H. Bluestein, 2012: The Second Verification of the Origins of Rotation in Tornadoes Experiment: VORTEX2. *Bull. Amer. Meteor. Soc.*, **93**, 1147–1170, doi:10.1175/BAMS-D-11-00010.1.
- Xue, M., M. Tong, and K. K. Droegemeier, 2006: An OSSE framework based on the ensemble square root Kalman filter for evaluating the impact of data from radar networks on thunderstorm analysis and forecasting. *J. Atmos. Oceanic Technol.*, **23**, 46–66, doi:10.1175/JTECH1835.1.
- Yussouf, N., and D. J. Stensrud, 2010: Impact of phased-array radar observations over a short assimilation period: Observing system simulation experiments using an ensemble Kalman filter. *Mon. Wea. Rev.*, **138**, 517–538, doi:10.1175/2009MWR2925.1.
- Ziegler, C. L., 1985: Retrieval of thermal and microphysical variables in observed convective storms. Part I: Model development and preliminary testing. *J. Atmos. Sci.*, **42**, 1487–1509, doi:10.1175/1520-0469(1985)042<1487:ROTAMV>2.0.CO;2.